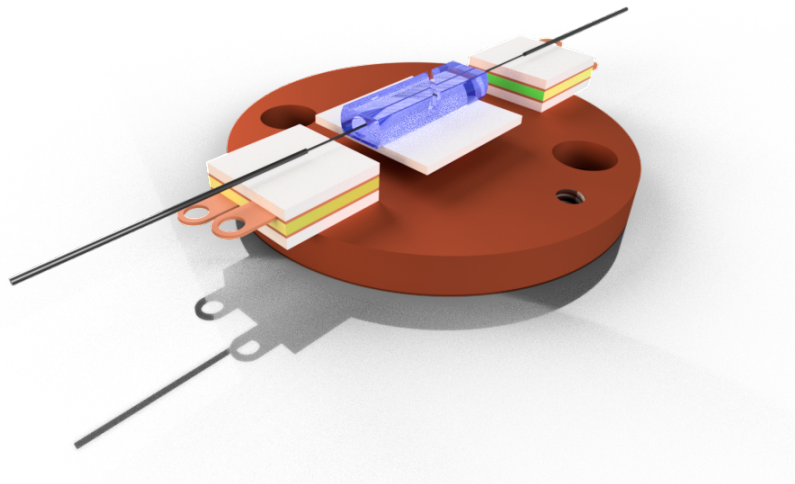


# Towards quantum non-linear optics with an atomically thin material and optical fibres

von  
Santhosh Surendra



Masterarbeit in Physik  
angefertigt im Physikalischen Institut

vorgelegt der  
Mathematisch-Naturwissenschaftlichen Fakultät  
der  
Rheinischen Friedrich-Wilhelms-Universität  
Bonn

March 2021

1. Gutachter : Prof. Dr. Michael Köhl
2. Gutachter : Prof. Dr. Stefan Linden

# Contents

<b>1</b>	<b>Introduction</b>	<b>5</b>
<b>2</b>	<b>Introduction to transition metal dichalcogenides (TMDC)</b>	<b>7</b>
2.1	General properties of TMDCs . . . . .	7
2.2	Optical properties of TMDCs . . . . .	8
2.2.1	Exciton response . . . . .	8
2.2.2	Thermal broadening of resonance . . . . .	10
2.3	Polariton system . . . . .	11
<b>3</b>	<b>TMDC experiment</b>	<b>13</b>
3.1	Design of the new experiment . . . . .	13
3.1.1	Transferring of monolayer onto an optical fibre . . . . .	14
3.1.2	The new assembly . . . . .	16
3.2	Spectroscopy setup . . . . .	17
3.2.1	Calibration of photodiodes . . . . .	19
3.2.2	Optical transfer matrix of the system . . . . .	19
3.3	Observations . . . . .	20
3.3.1	Cryostat properties . . . . .	20
3.3.2	Spectroscopic results . . . . .	21
<b>4</b>	<b>Single-shot micro-fabrication</b>	<b>25</b>
4.1	Setup . . . . .	25
4.1.1	Spatial filtering . . . . .	25
4.2	Free shooting parameters . . . . .	27
4.3	Modelling of laser ablation . . . . .	28
4.4	Experimental verification of the model . . . . .	31
<b>5</b>	<b>Multi-shot micro-fabrication</b>	<b>33</b>
5.1	Simple application of multiple shots . . . . .	33
5.1.1	Ellipticity control . . . . .	33
5.1.2	Laser polishing . . . . .	33
5.2	Non-linearity of multiple shots . . . . .	35
5.2.1	Off-centre shots . . . . .	35
5.2.2	Superimposed shots . . . . .	36
5.2.3	Displaced shots – laser dot milling . . . . .	36
5.3	Towards complete automation . . . . .	37
5.3.1	Final setup with additional updates . . . . .	38
5.3.2	New python experimental control . . . . .	40
<b>6</b>	<b>Conclusion and outlook</b>	<b>41</b>
<b>A</b>	<b>Fibre shooting process</b>	<b>43</b>
A.1	New python application . . . . .	43
A.2	Procedure . . . . .	44

<b>B Displaced shots illustrations</b>	<b>47</b>
<b>References</b>	<b>51</b>
<b>Acknowledgements</b>	<b>55</b>

# Chapter 1

## Introduction

In the early 20<sup>th</sup> century, Max Plank [1] and Albert Einstein [2] introduced the concept of “light quanta”, forever changing the course of Physics. These particles that light is made of were later named “Photons” by Gilbert Lewis [3] in 1926. Though it was an abstract idealism, science and technology have evolved significantly since then and we now have sources that produce single photons. A single photon source is a quantum state of light that has significant scientific importance [4]. Furthermore, such a light source has immense applications in the fields of quantum information science, quantum cryptography, and quantum repeaters. Currently there are single photon sources based on neutral atoms [5], ions [6], NV centres in diamonds [7], Quantum dots [8], and many more. These are all bulky instruments that require trained professionals to operate. In this thesis, we aim to design and build a robust fibre coupled single photon source using a 2 dimensional material.

Since the isolation of graphene [9], numerous two dimensional materials have been fabricated. Monolayers of transition metal dichalcogenides are semiconductors, with a band gap in the optical regime. These materials have strong optical response owing to the formation of excitons [10]. It is predicted that when such a monolayer is placed in vicinity of a broadband mirror, the excitons strongly interact with themselves and the incident light, resulting in a non-linear optical response. The transmitted light from such a system is predicted to be a single photon source [11]. However, such a system has not been experimentally realised yet.

There are certain physical challenges that must be overcome to build such a system. After analysing the drawbacks from the previous experiments [12, 13], I asked the question:

**Is it possible to fabricate and transfer a monolayer onto the end faced of an optical fibre?**

If the monolayer is over the core of a single mode optical fibre, one can efficiently illuminate it from the fibre. If such a transfer process is possible, we have to determine the resonance properties of our specific flake and its temperature dependence before utilising it efficiently. Thus, we must answer

**How does the exciton resonance change with respect to temperature for our flake?**

before proceeding with the experiment. Once this is done, we must build a TMDC - mirror resonator whose length is in order of a  $\mu\text{m}$ . We can build a fibre-fibre resonator with a second fibre coated with reflective metal. Fibres allow us to fabricate such short resonators. This can replicate the system we desire, and also make it inherently fibre coupled! Our research group specialises in building optical fibre based resonators [14, 15, 16]. We fabricate concave structures on fibre-end facets using a  $\text{CO}_2$  laser, following [17]. Meanwhile, there was a general research interest for having large concave structures with radius of curvature in order of a mm on macroscopic glass substrates. Thus, to understand the complete potential of our setup, I asked the question:

## **What are the limits achievable with the current setup?**

Following this, I had to tackle the question:

### **How in general can the CO<sub>2</sub> laser fabrication experiment be improved?**

In this theses, I describe the journey I took to tackle, and answer these questions. Various problems were discovered, and solved during the process. In chapter 2, I introduce the theoretical background for transition metal dichalcogenides (TMDC/TMD), and our single photon source experiment. Chapter 3 describes the design, fabrication, and spectroscopy of TMDC monolayers on optical fibres. I characterise the CO<sub>2</sub> laser fabrication setup, and present some interesting observations in chapter 4. In chapter 5, I describe various challenges I encountered with the experiment, and how I attempted to overcome them. I conclude with chapter 6 presenting some outlooks for the projects I undertook.

## Chapter 2

# Introduction to transition metal dichalcogenides (TMDC)

Numerous 2D materials have been found that possess a broad range of electrical, thermal, and optical properties. Insulators [18], semiconductors [19], and (semi)metals [9] have been discovered so far. Of these, transition metal dichalcogenides (TMDCs or TMDs) are of special importance as these are semiconductors with band gaps similar to Si and GaAs crystals (1 eV – 2 eV). This gives them interesting optical and electrical properties [20].

Section 2.1 describes the physical properties of TMDCs, and section 2.2 explains their optical responses. In section 2.3, the end goal of our experiment is described, based on which the rest of this thesis is built upon.

### 2.1 General properties of TMDCs

Bulk TMDCs are made of layers of atoms with very strong intra layer bonding. Multiple layers are held together by weaker van der Waals force. TMDCs consist of transition metals (M): Molybdenum (Mo) and Tungsten (W), and chalcogenide atoms (X): Sulphur (S), Selenium (Se), Tellurium (Te). Their general chemical formula is given by  $MX_2$ . In this work, we use  $MoSe_2$  monolayers, and from here on it will be used synonymously with TMDCs.

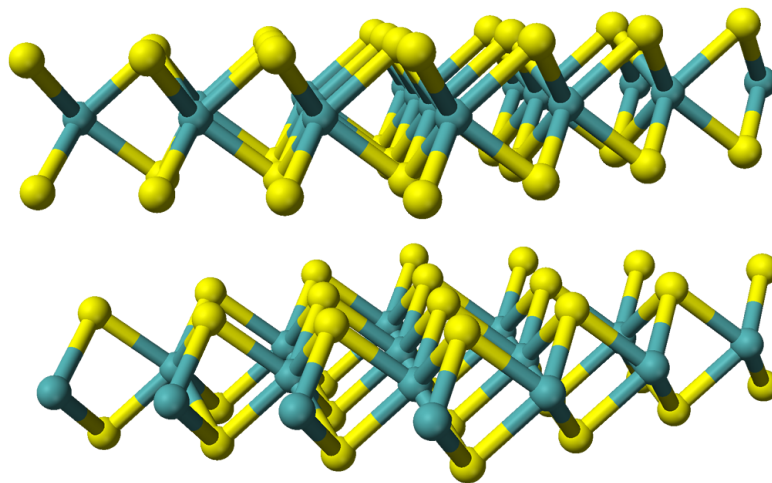


Figure 2.1: Crystal structure of  $MoSe_2$ . Green spheres denoting Mo atoms, and yellow spheres denoting Se atoms. Image taken from [21].

In a single layer, heavy Mo atoms are arranged in a triangular lattice, and are sandwiched between two layers of Se atoms. These are also arranged in a displaced triangular lattice, as shown in Figure 2.2. The average distance between Mo atoms is  $3.288 \text{ \AA}$  and the thickness of a layer is  $3.328 \text{ \AA}$  [22]. In-plane reciprocal lattice is a honeycomb structure with first Brillouin zone (BZ) being a hexagon. High symmetry points in the Brillouin zone are the centre of hexagon ( $\Gamma$ ), vertices ( $K$  and  $-K$ ), and centres of sides in the hexagon ( $M$ ). The first Brillouin zone is illustrated in Figure 2.2.

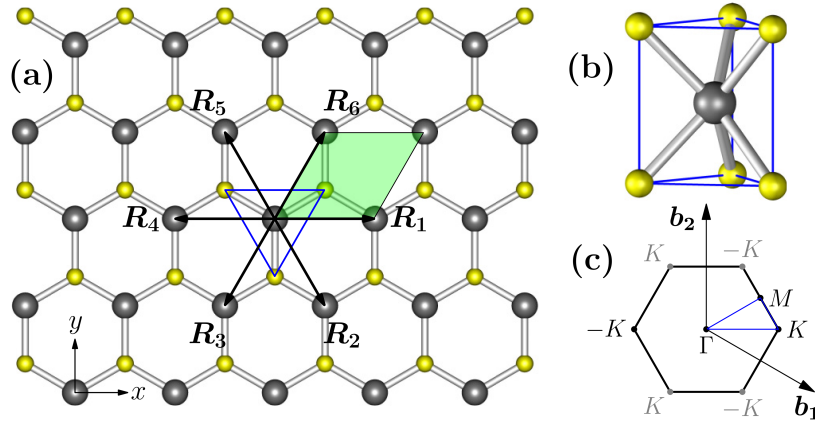


Figure 2.2: (a) In plane crystal lattice of  $\text{MoSe}_2$ , with the green region illustrating a unit cell.. (b) Actual unit cell of our monolayer in 3D. (c) The first Brillouin zone of the in-plane lattice. Figure taken from [23].

## 2.2 Optical properties of TMDCs

Monolayer  $\text{MoSe}_2$  has a direct band gap at  $K$  and  $-K$  points in its BZ. This gives it interesting optical properties such as photo-luminescence [24]. In a monolayer, inversion symmetry is broken, leading to valley dependent optical selection rules [25]. Owing to  $d$  orbitals from heavy Mo atoms, there is a strong spin-orbit coupling, resulting in splitting of valence and conduction bands at  $K$  and  $-K$  points in the BZ. Splitting of valence bands are in order of  $100 \text{ meV}$  and conduction band is in order of several  $\text{meV}$ . Hence, with appropriate external electric fields and polarisation, one can excite specific valley and spin degrees of freedom efficiently [26].

Optical properties can be understood well using the concept of excitons [10]. When an electron in the valence band absorbs radiation of energy higher than the band gap, it can excite to the conduction band, leaving a vacancy behind. This vacancy behaves as a particle of positive charge, with an effective mass in the crystal, known as hole. Conducting electrons can form a bound state with a hole (similar to a hydrogen atom or positronium) forming a quasi particle known as exciton [27]. Excitons exist only in a crystal, and hence is quantum confined to 2 dimensions in our case. More exotic quasi particles can also form when excitons form bound states with other electrons or holes, like trions (exciton + electron or hole), bi-exciton (exciton + exciton), etc. However, formation of these exotic quasi particles is heavily suppressed at higher temperatures.

### 2.2.1 Exciton response

In monolayer  $\text{MoSe}_2$ , due to splitting of valence and conduction bands, excitons of lower (A) and higher (B) energies can form, as illustrated in Figure 2.3, and Figure 3.1. At room temperature, A excitons have their resonance at  $(782 \pm 5) \text{ nm}$ , and shifts to about  $(750 \pm 5) \text{ nm}$

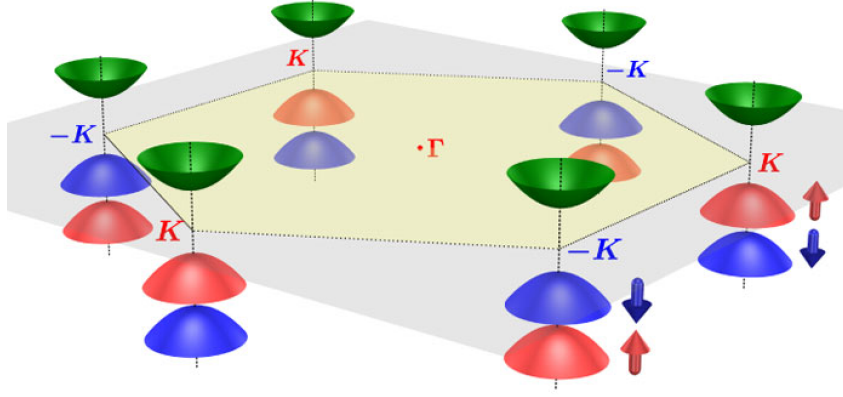


Figure 2.3: Spin-orbit splitting of valence band at K and -K points. A excitons form by coupling of higher valence band with the conduction band (green), and B excitons form by coupling of lower valence band with the conduction band. Figure taken from [26]

at 0 K [28, 29, 30]. Our research group has good lasers available in this spectral range, and hence we choose monolayers of MoSe<sub>2</sub> and its A exciton resonance in this work.

Since Excitons are displaced charges with an electric dipole moment, one can model their optical response using the driven Lorentz oscillator model [31]. Since they are confined to 2 dimensions in a monolayer, for normal incidence of light, radiative decay is heavily suppressed along transverse directions, making TMDCs an ideal oscillator coupled to a 1D channel. The reflectance and transmittance coefficient for an ideal exciton resonance is then given by 2.1 [32]:

$$r_{\text{TMD}_{\text{ideal}}}(\omega; \omega_0, \gamma) = \frac{-i\frac{\gamma}{2}}{(\omega - \omega_0) + i\frac{\gamma}{2}} \quad \text{and} \quad t_{\text{TMD}_{\text{ideal}}}(\omega; \omega_0, \gamma) = \frac{(\omega - \omega_0)}{(\omega - \omega_0) + i\frac{\gamma}{2}} \quad (2.1)$$

where  $\omega$  is the angular frequency of the radiation field,  $\omega_0$  is the resonance frequency of the exciton, and  $\gamma$  is the radiative line width. Non radiative decay is however still possible due to thermal phonons, and formation of dark excitons (excitons in an indirect band gap) [33]. This can be included phenomenologically as a line broadening mechanism, with an effective line width  $\gamma \rightarrow (\gamma + \gamma')$  where  $\gamma'$  is the non-radiative line width. A useful parameter to quantify the non-radiative decay in the system is given by 2.2:

$$\eta = \frac{\gamma}{\gamma + \gamma'} \quad (2.2)$$

Including a non radiative decay channel, one obtains the expression for reflectance as 2.3 [32, 11]:

$$r(\omega; \omega_0, \gamma, \gamma') = \eta \cdot r_{\text{ideal}}(\omega; \omega_0, \gamma + \gamma') \quad (2.3)$$

Thus, Equation 2.3, 2.1 and 2.2 together gives Equation 2.4:

$$r_{\text{TMD}}(\omega; \omega_0, \gamma, \gamma') = \frac{-i\frac{\gamma}{2}}{(\omega - \omega_0) + i\frac{\gamma + \gamma'}{2}} \quad \text{and} \quad t_{\text{TMD}}(\omega; \omega_0, \gamma, \gamma') = \frac{(\omega - \omega_0) + i\frac{\gamma'}{2}}{(\omega - \omega_0) + i\frac{\gamma + \gamma'}{2}} \quad (2.4)$$

One can see from Equation 2.1 that when no non-radiative decay channels are available, the TMDC acts as a perfect reflector at resonance, although it is atomically thin! When non-radiative decay is included, as in Equation 2.4, absorption is increased at resonance, and there

is no perfect reflectivity any more. Absorption is defined by the relation  $A = 1 - R - T$ , where  $R = |r|^2$ , and  $T = |t|^2$  are reflection and transmission intensities respectively. Figure 2.4 illustrates the changes in  $R$ ,  $T$ , and  $A$  at resonance for varying  $\gamma'$  and  $\eta$ <sup>1</sup>. Thus, for observing large reflectance, following condition has to be met 2.5:

$$\eta \approx 1 \Leftrightarrow \gamma \gg \gamma' \quad (2.5)$$

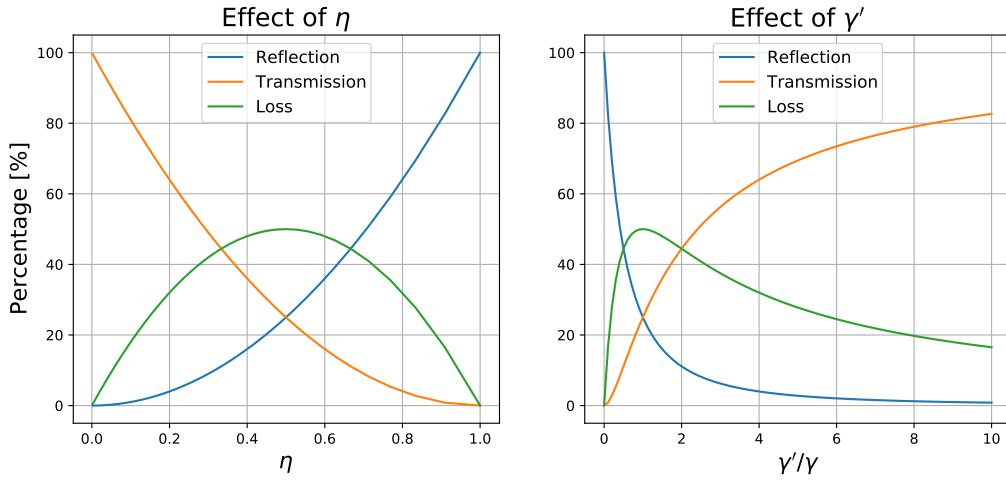


Figure 2.4: Variation of power reflection, transmission and absorption coefficients with  $\eta$  and  $\gamma'$ .

## 2.2.2 Thermal broadening of resonance

From [33], we know that the largest decay mechanism is by thermal phonons. The temperature dependent line width due to phonons of angular frequency  $\omega_{\text{ph}}$  at a temperature  $T$  is given by [33]:

$$\gamma_{\text{phonon}}(T) = \gamma_1 T + \frac{\gamma_2}{\exp\left(\frac{\hbar\omega_{\text{ph}}}{k_B T}\right) - 1} \quad (2.6)$$

where  $\gamma_1$  is the coupling to acoustic phonons, and  $\gamma_2$  is due to other intra valley optical phonon scattering. The denominator in Equation 2.6 comes from Bose-Einstein statistics. For MoSe<sub>2</sub>,  $\omega_{\text{ph}}$  is about 30 THz [34, 24]. Thus, temperature dependent line width of our system is then given by Equation 2.7:

$$\begin{aligned} \gamma(T) &= \gamma_0 + \gamma_{\text{phonon}}(T) \\ &= \gamma_0 + \gamma_1 T + \frac{\gamma_2}{\exp\left(\frac{\hbar\omega_{\text{ph}}}{k_B T}\right) - 1} \end{aligned} \quad (2.7)$$

where  $\gamma_0$  is the radiative line width of the resonance. Comparing Equation 2.7 with our definition for  $\gamma'$ , we have  $\gamma' = \gamma_{\text{phonon}}(T)$ . Thus, to satisfy the condition 2.5, we must cool down the sample to a very low temperature.

<sup>1</sup>PYTHON packages Numpy, Scipy, and Matplotlib were used for data analysis and plotting throughout this work.

## 2.3 Polariton system

Due to exciton-exciton interactions in the crystal, resonance frequency shifts locally. Because of this, there is a slight deviation from the above model, and transmission is non zero at resonance even for an ideal TMDC [32]. Interestingly, it is predicted that the transmitted light in this case is in a multimode squeezed state [32]. The exciton resonances are however still quite broad compared to other systems such as atoms and quantum dots – in order of THz.

To enhance the quantum properties of bare TMDC, Wild et al. [11] considered a system described in Figure 2.5. In this configuration, a broad band reflective mirror is placed in the vicinity of a monolayer.

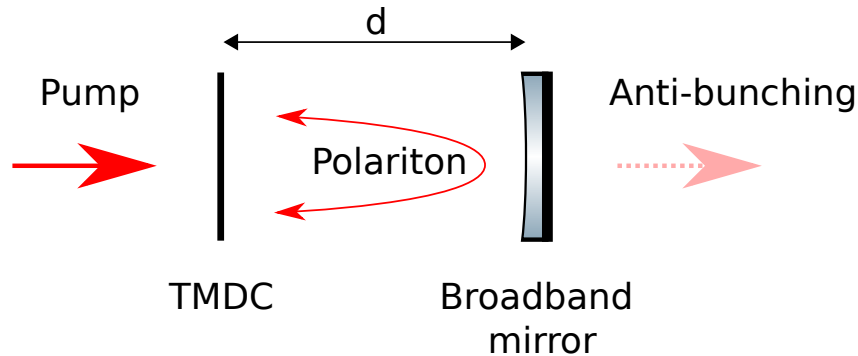


Figure 2.5: The polariton system that we aim to achieve in our laboratory. Figure reproduced from [11].

Following criteria were assumed to be met:

- The TMDC is pumped by a coherent state of light (LASER) near resonant with the monolayer.
- Reflectivity of the mirror is same as that of the monolayer on resonance.
- Spacing between the mirror and monolayer is a specific multiple of the wavelength used, as mentioned in [11].
- The spacing is in order of a wavelength (the multiple from the previous point is in order of unity).

A LASER pump was assumed for convenience. The matching of reflectivity assures impedance matching of the resonator, resulting in maximum transmission of photons [35]. With the spacing in order of wavelength, a photon emitted by the monolayer can reflect off the mirror and interact with itself within the decay time of excitons. It is similar to Purcell effect [36], resulting in formation of an exciton-photon superposition. This can be considered as a new quasi particle called “exciton-polariton” [37]. Such a system reduces the line width of the emitters (excitons) causing stronger coupling between light and matter. The spacing cannot be an integer multiple of the pump wavelength as that would result in nodes forming on the mirror and the monolayer. Since there is no electric field oscillation in the nodes, the monolayer cannot respond to the field, and the system will not be useful. The exact spacing is derived in [11]. The transmitted light field from such a system is simulated to be anti-bunched, resulting in a single photon source. The end goal of our experiment is to realise such a state in our laboratory.



# Chapter 3

## TMDC experiment

In chapter 2, we understood the properties of an exciton resonance in MoSe<sub>2</sub> monolayer. In order to use a monolayer in the experiment effectively, one must first know the resonance properties of the flake being used, as each sample is unique. This stems from the fact that crystal defects can form during the preparation process. Thus, the first thing to do after having a monolayer is to perform spectroscopy on it to understand the resonance parameters. Next thing to do in the experiment is to make a polariton system as mentioned in section 2.3. Thus, we must design and build a setup where both spectroscopy, and single photon source can be done without much modifications.

In section 3.1, we discuss the drawbacks of the old design from [13, 12], and how we built the new one. Section 3.2 describes the experimental setup for performing the spectroscopy of the sample at cryogenic temperatures. In section 3.3, observations are presented from the performed spectroscopy.

### 3.1 Design of the new experiment

Before designing a new assembly, one must first understand the drawbacks from previous experiments [13, 12]. Monolayer samples were previously transferred onto a silica substrate, and were analysed through the window of a cryostat <sup>1</sup>. Following drawbacks were observed for this configuration:

- It was difficult to find the monolayer using just a narrowband laser beam at room temperature. Hence, it was difficult to align the flake with the cryostat window, and maintain the alignment during cool down.
- Thin silica substrate was good for the cryostat owing to its small mass, but caused strong interference during laser spectroscopy.
- The thin cryostat window acted as another etalon, and caused further interference effects.
- The laser spot diameter was about 12 μm on the sample, hence could easily illuminate the surroundings of monolayer, adding noise to the signal.
- For second stage of the experiment, it was not clear on how to place a moveable mirror close enough to a monolayer. One needs to be able to move the mirror in a precise fashion in order to select the correct TMDC-mirror distance. Previous attempt was to scan the length of resonator by changing the temperature, but it did not work well as the resonance changed in the scan regime.

---

<sup>1</sup>Konti-Cryostat-Mikro

### 3.1.1 Transferring of monolayer onto an optical fibre

After understanding the drawbacks from the previous design, we decided to transfer a monolayer onto the end facet of a single mode (SM) optical fibre. A cleaved optical fibre will have a very high quality flat surface, making it a good candidate for the transfer process. Furthermore, if the monolayer flake is positioned right on the core of a SM fibre – which is about  $5\ \mu\text{m}$ , one can selectively illuminate the monolayer efficiently. The fibre has very small mass, making it cryostat compatible. Our research group specialises in building fibre optical resonators with lengths in order of tens of  $\mu\text{m}$  [14, 15, 16], making such a system ideal for our current purpose. But, the big question still stood:

#### Is it possible to transfer a monolayer $\text{MoSe}_2$ onto the end facet of a SM optical fibre?

To answer this, we must first understand the preparation and transferring process of monolayers used in our institute at the research group headed by Prof. Dr. Stefan Linden <sup>2</sup>. We use the method of mechanical exfoliation and dry viscoelastic stamping as described in [38]. The following steps summarises the preparation of a monolayer, as illustrated in Figure 3.2:

1. Add some mm sized flakes of  $\text{MoSe}_2$  crystal onto a scotch tape, and cover it with a second piece of scotch tape.
2. Rapidly pull them apart, exfoliating the crystals. Repeat the procedure until very thin flakes are left on the tape. Such an exfoliation scheme works as the bulk crystals are made of monolayers held together by weak van der Waals bonds, as described in section 2.1.
3. Place a piece of Polydimethylsiloxane (PDMS) tape (around  $1\ \text{cm}^2$ ) on the exfoliated crystal chunks, and gently pull them apart. This transfers some crystals of  $\text{MoSe}_2$  onto PDMS. PDMS has a velocity and temperature dependent adhesion. Hence, one can separate the samples from PDMS by choosing the correct ambient temperature and peeling velocity.
4. Mount the PDMS onto a microscope with reflection illumination, and inspect the crystals on the PDMS.
5. Based on contrast, one can visually identify the candidates for a monolayer.

To verify whether the flake is a monolayer, we perform a reflection spectroscopy using a halogen lamp. We illuminate the entire PDMS, and select the region of interest using an iris. Reflection spectra of monolayer and bare PDMS are acquired using a high resolution spectrometer. The normalised spectra following 3.1 determines whether the sample is a monolayer or not [28, 29].

$$R = \frac{R_{\text{TMD}} - R_{\text{PDMS}}}{R_{\text{TMD}}} \quad (3.1)$$

where  $R_{\text{TMD}}$  and  $R_{\text{PDMS}}$  are reflection spectra from the sample and PDMS respectively. If the low energy resonance (A exciton from section 2.2) is located at  $(782 \pm 5)\ \text{nm}$ , then it implies that the sample is a monolayer. Otherwise, we reject it and start over. Normalised reflectance of our sample is shown in Figure 3.1.

Once we have a monolayer  $\text{MoSe}_2$  on the PDMS, the next step is to transfer it onto a substrate of choice, and in our case: an end facet of a SM optical fibre. We choose acrylate coated SM fibres from Thorlabs <sup>3</sup>. The fibre was prepared by stripping the coating to about 5mm at one end, and then by cleaving. It was mounted onto a magnetic fibre holder, and was fixed onto a 3-axis micrometer translation stage for fine alignment. The fibre was illuminated from the back using a green LED as a marker for placement of the flake. PDMS was mounted onto a

---

<sup>2</sup><https://www.nanophotonik.uni-bonn.de/>

<sup>3</sup>S630-HP

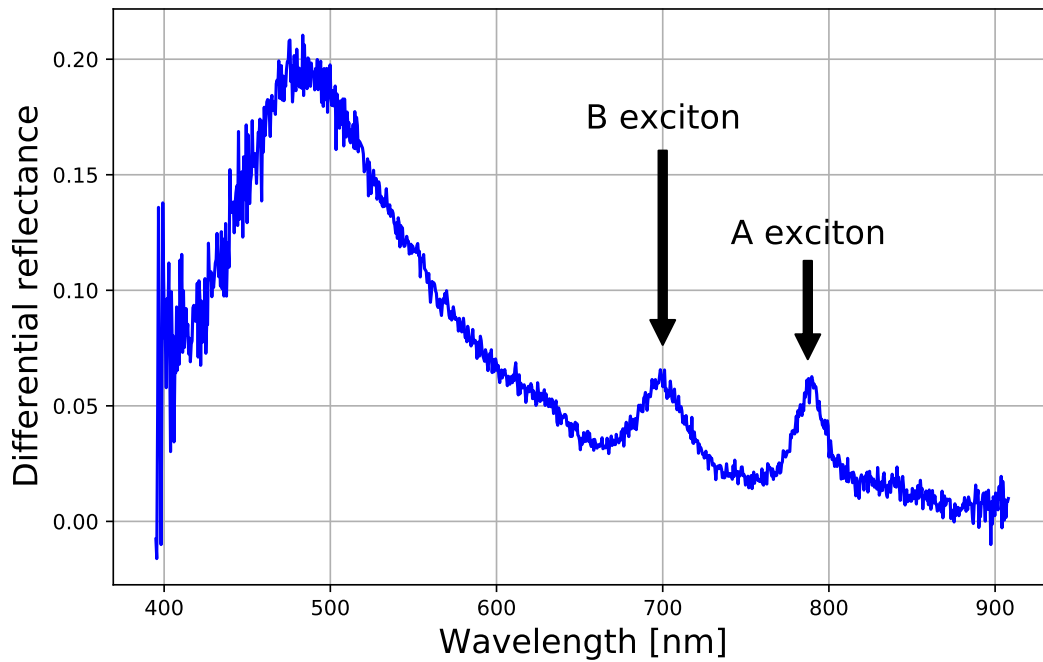


Figure 3.1: Normalised reflectance spectra at room temperature. A-exciton resonance is around 777 nm confirming that the flake is a monolayer MoSe<sub>2</sub>.

second 3-axis translation stage just above the fibre, as shown in Figure 3.3. The overall process is illustrated in Figure 3.2, where one can replace the pink substrate by an optical fibre.

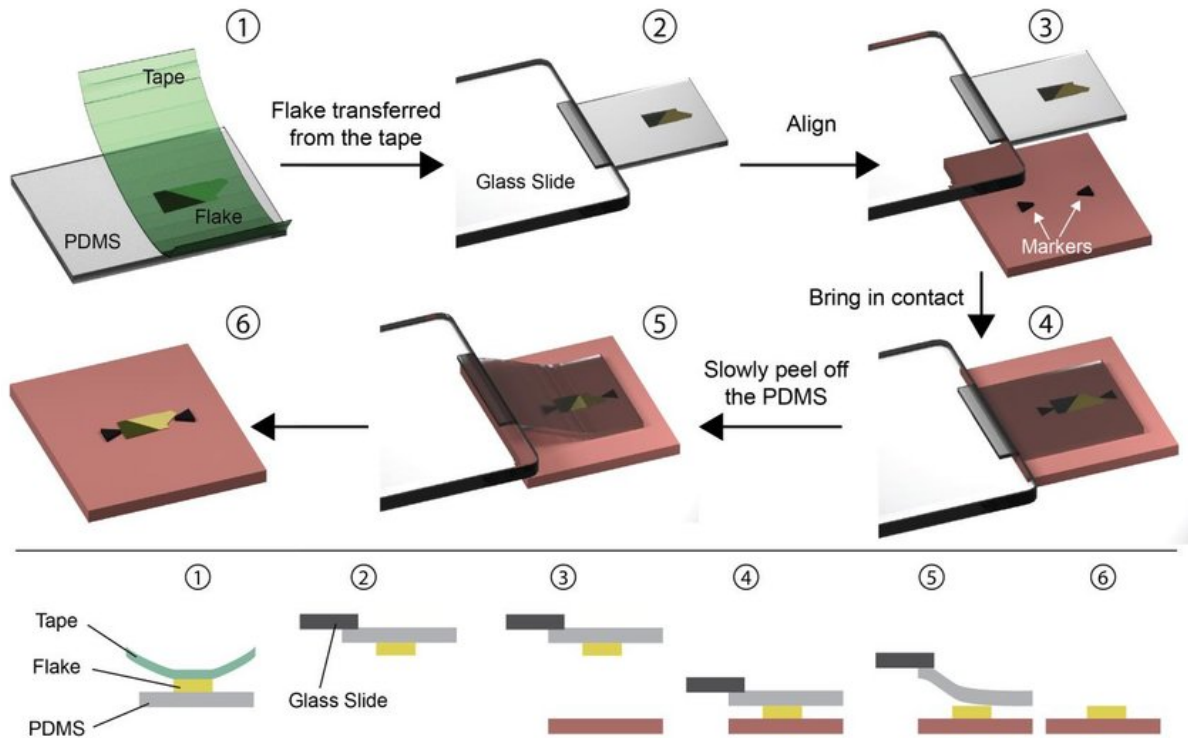


Figure 3.2: Transfer process of monolayers. Image taken from [39]. In this thesis, we used an end facet of an optical fibre instead of the pink substrate that is illustrated.

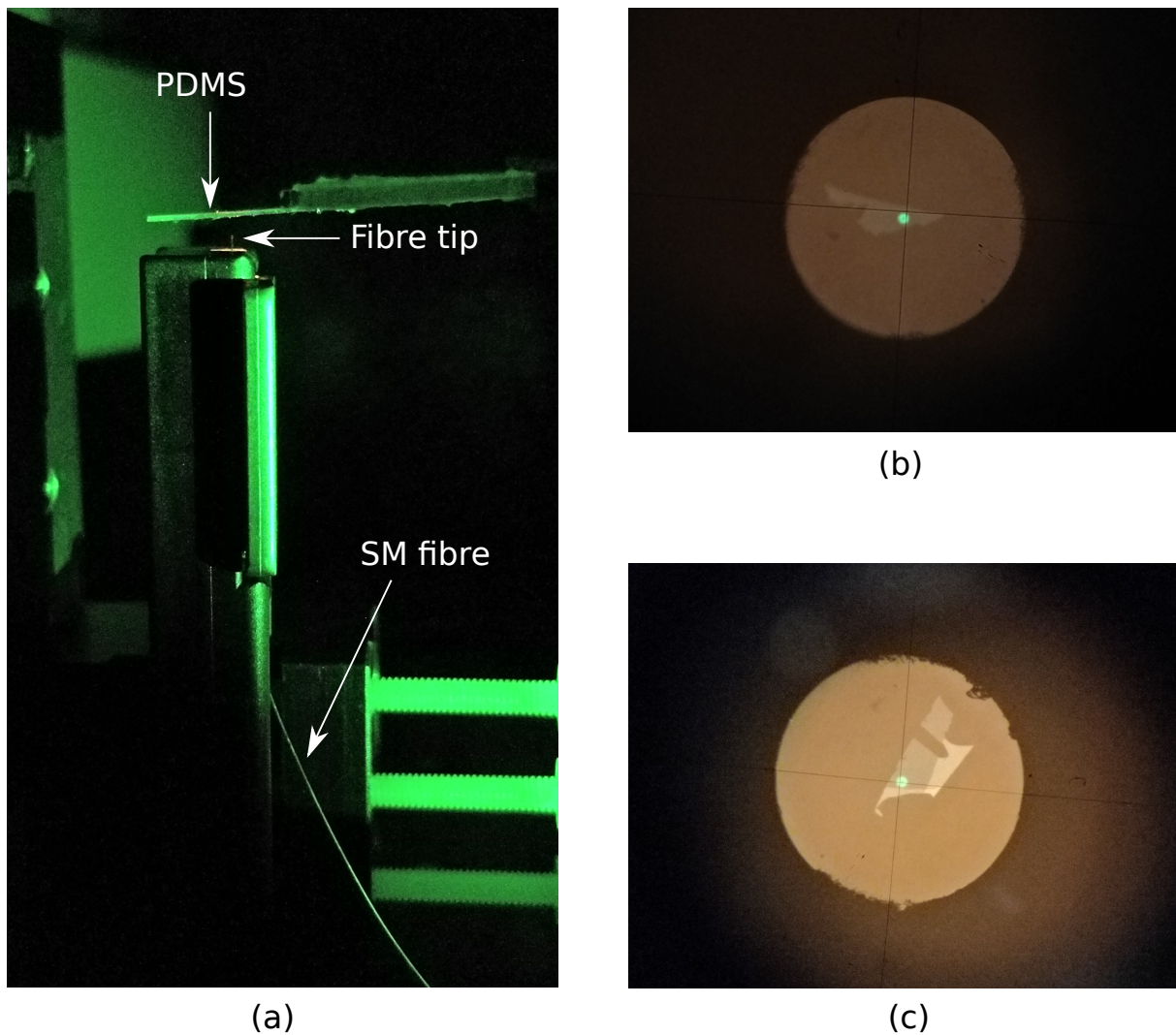


Figure 3.3: (a) Assembly to transfer the monolayers onto a SM fibre end facet. (b), (c) Transferred monolayers on single mode optical fibre. A green LED was used to illuminate the fibre from behind, so core can be aligned with the monolayer.

Using the illumination from fibre core as reference, the core was aligned with the monolayer using a high magnification microscope. Slowly, the two were brought into contact with each other, and the transfer was carried out by gently separating them. Figure 3.3 shows successfully transferred monolayers onto a SM fibre.

### 3.1.2 The new assembly

Now that we can produce fibres with monolayers on them, the next step is to design a new assembly for the experiment. We had to consider the following challenges while designing the new assembly:

- Both spectroscopy, and the single photon-source generation should be performed with the same assembly, without major modifications.
- Alignment must be maintained at all temperatures. As we reach cryogenic temperatures, various components can thermally contract and misalign with respect to each other.
- Since the new system involves optical fibres, they should somehow be brought out of the cryostat for fibre coupling.

Keeping the above points in mind, we designed the assembly illustrated in Figure 3.4. A glass ferrule was considered to maintain alignment of the fibres. As we create a vacuum in the cryostat for removing any water vapour and for thermal insulation, we cut an angled slit onto the glass ferrule for any air between the fibres to escape. This was done using a diamond wire. The angle was about  $45^\circ$  so no strong flexure occurs as temperature is varied. A second Multimode (MM) optical fibre<sup>4</sup> could detect the transmission signal of TMDC. Because of its large core size and high numerical aperture, transmitted (and diverging) light from the SM fibre could be efficiently collected with a MM fibre. Two shear piezo-electric actuators were used for fine movement of the fibres.

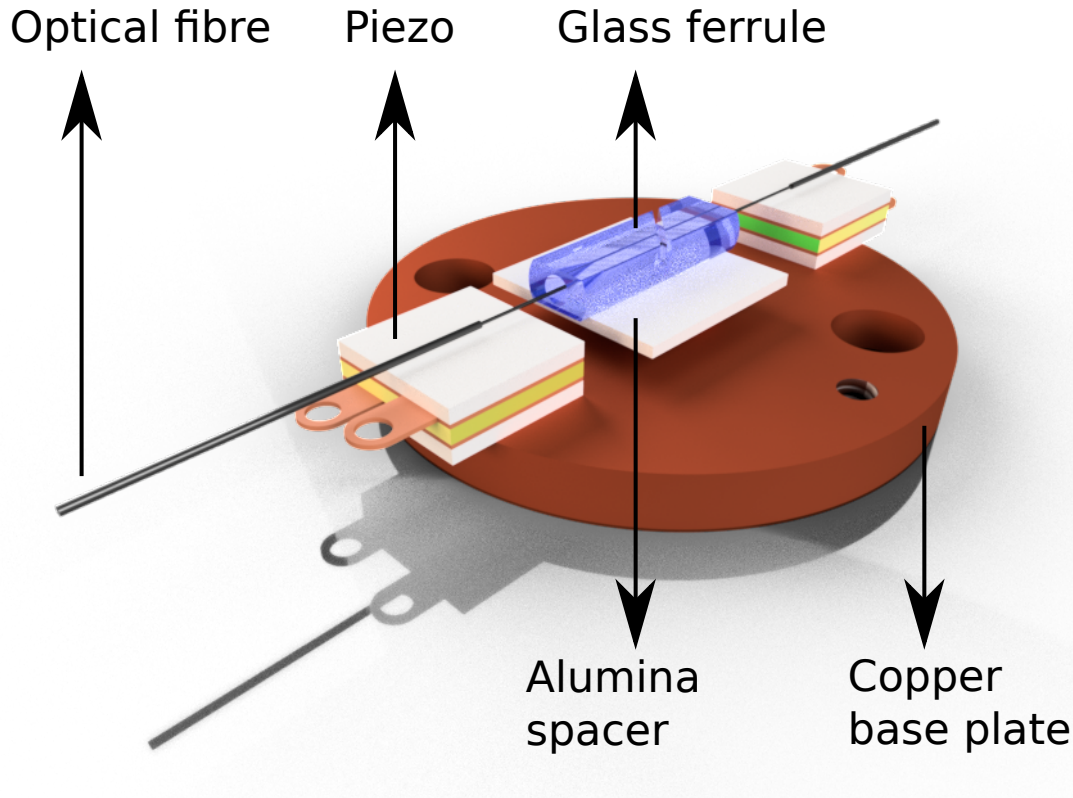


Figure 3.4: Main assembly of the TMDC experiment. Designed and rendered using Autodesk Inventor 2020.

The two fibres were glued onto shear piezos as shown in the design. The copper base plate was re-used from the previous setup, so, an alumina plate was glued between the ferrule and the base plate for height adjustment. All components were fixed using Stycast<sup>5</sup> with catalyst 9 bonding agent. The fibres were inserted into the ferrule using 5-axis micrometer stages and were bonded onto the shear piezo using superglue. The superglue can be dissolved using acetone, so we can remove the multimode fibre after spectroscopy is performed. For the second step of experiment, a gold coated fibre can be inserted back into the ferrule forming the required polariton assembly. The completed assembly with SM and MM fibres is shown in Figure 3.5.

## 3.2 Spectroscopy setup

With the assembly inserted into cryostat, fibres were pulled out through  $300\ \mu\text{m}$  holes drilled on the lid, and were spliced with appropriate patch cables. In order to perform spectroscopy,

<sup>4</sup>FG105LCA from Thorlabs

<sup>5</sup>LOCTITE STYCAST 2850FT

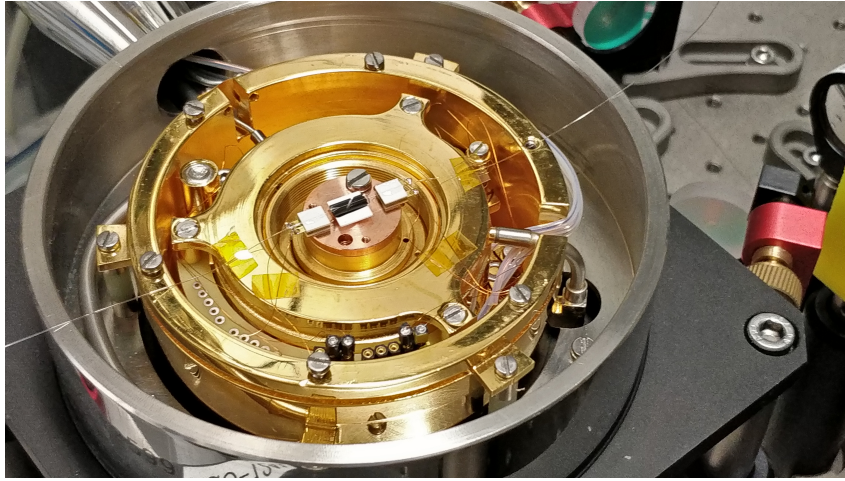


Figure 3.5: Complete spectroscopy assembly inside the cryostat.

the setup illustrated <sup>6</sup> in Figure 3.6 was built .

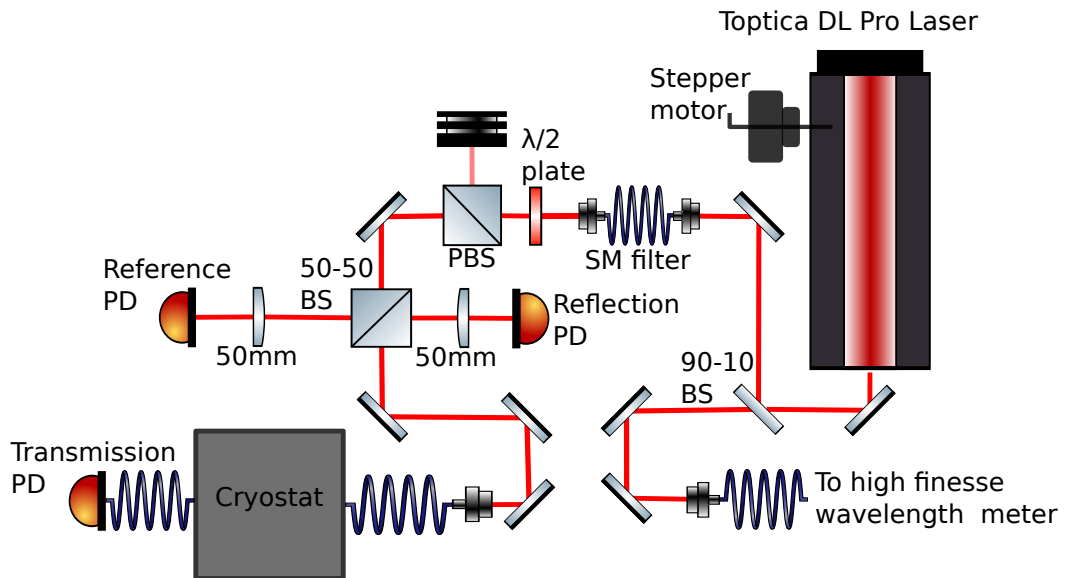


Figure 3.6: Spectroscopy setup of the TMDC experiment.

An external cavity diode laser <sup>7</sup> was considered for this purpose. Using a home built stepper motor assembly with a hex-key, the grating angle could be changed via a computer, providing a wavelength scan range from around 753 nm to 786 nm. To determine the wavelength, 10% of light was diverted to a high-finesse wavelength meter <sup>8</sup>. The rest was spatially filtered using a SM fibre. Power from the SM fibre was controlled using a polarising beam splitter (PBS) and a half wave plate.

The diode laser's output power fluctuated as the wavelength was scanned. To compensate for this, half of the light after PBS was diverted onto a photodiode as power reference. The other half was sent to the SM fibre for spectroscopy. Transmitted light through the MM fibre was measured using a second photodiode, and the reflected light through the SM fibre

<sup>6</sup>Alexander Franzen – <http://www.gwoptics.org/ComponentLibrary/>. Same library is used through out this thesis

<sup>7</sup>TOPTICA DL pro with Eagleyard photonics gain chip

<sup>8</sup>High-Finesse WS-6

was re-diverted onto a third photodiode by the 50-50 beam splitter. The reflected signal was reduced by about half by the beam splitter, and this effect was compensated during data analysis.

### 3.2.1 Calibration of photodiodes

Following effects had to be compensated for during the data analysis:

- Power fluctuations during the scan process.
- Diode dark currents.
- The deviations of reflected and transmitted power from 50%, as the beam splitter wasn't an ideal one.
- Different gain settings on the three diodes.
- Reduction of power in reflection path due to the 50-50 BS.
- Fibre coupling efficiency due to the broad scan range.

Appropriate weights for diode signals were acquired for each of the above effects, and used during the analysis step. Once the diode signals were measured, reflection and transmission spectra were obtained using the relation 3.2:

$$R = \frac{(V - V_{\text{dark}})_{\text{reflection}} \cdot \eta_{\text{reflection}}}{(V - V_{\text{dark}})_{\text{reference}} \cdot \eta_{\text{reference}}} \quad \text{and} \quad T = \frac{(V - V_{\text{dark}})_{\text{transmission}} \cdot \eta_{\text{transmission}}}{(V - V_{\text{dark}})_{\text{reference}} \cdot \eta_{\text{reference}}} \quad (3.2)$$

where  $\eta_{\text{reference}}$ ,  $\eta_{\text{reflection}}$ , and  $\eta_{\text{transmission}}$  are the obtained weights from the above considerations.

### 3.2.2 Optical transfer matrix of the system

The primary optical assembly consists of a SM fibre, a MM fibre, and the TMDC monolayer, as illustrated in Figure 3.7. Since everything is mounted on a copper base plate, as the temperature is lowered, the baseplate contracts, bringing the two fibres closer. Thus, the fibres were glued onto the piezos with a separation of about 120  $\mu\text{m}$  at room temperature of 292 K. As the system contracts, the gap between fibres would reduce to about 50  $\mu\text{m}$  at 4 K [13]. The two cleaved faces of the fibres would form an etalon imposing an interference pattern onto our spectra. This can be simulated using transfer matrix formalism [35, 40]. We however used a phenomenological model from 3.3 to remove the oscillations due to etalon from our data.

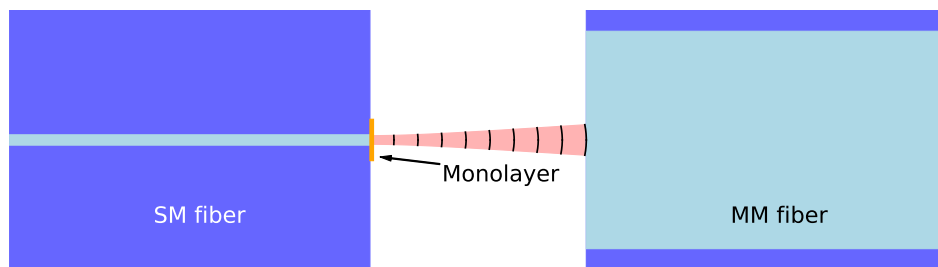


Figure 3.7: Optical system of spectroscopy setup. All components are in scale except for the monolayer.

### 3.3 Observations

With everything in place, the next step of the experiment was to perform spectroscopy on our sample at cryogenic temperatures.

#### 3.3.1 Cryostat properties

The cryostat was evacuated to  $10^{-3}$  mbar. This extracted any water vapour inside, and provided good thermal insulation. As a first step, we used liquid nitrogen for cooling. The temperature was changed with a ramp of about 1 K per minute through out the experiment. Such a rate was chosen to reduce any flexures in the components inside the cryostat. Figure 3.8 illustrates a typical cooling cycle of the cryostat. One can observe the rate is slow initially, owing to themalisation of the flow tubes inside the cryostat. After about 25 min, all pipes thermalise with the flowing nitrogen, and the system stabilises with the PID controller.

Heating of the cryostat to room temperature was performed naturally, by stopping the nitrogen flow. Internal heaters with PID feedback heated it up at a ramp of about 1 K per minute. Figure 3.8 shows a typical heating cycle.

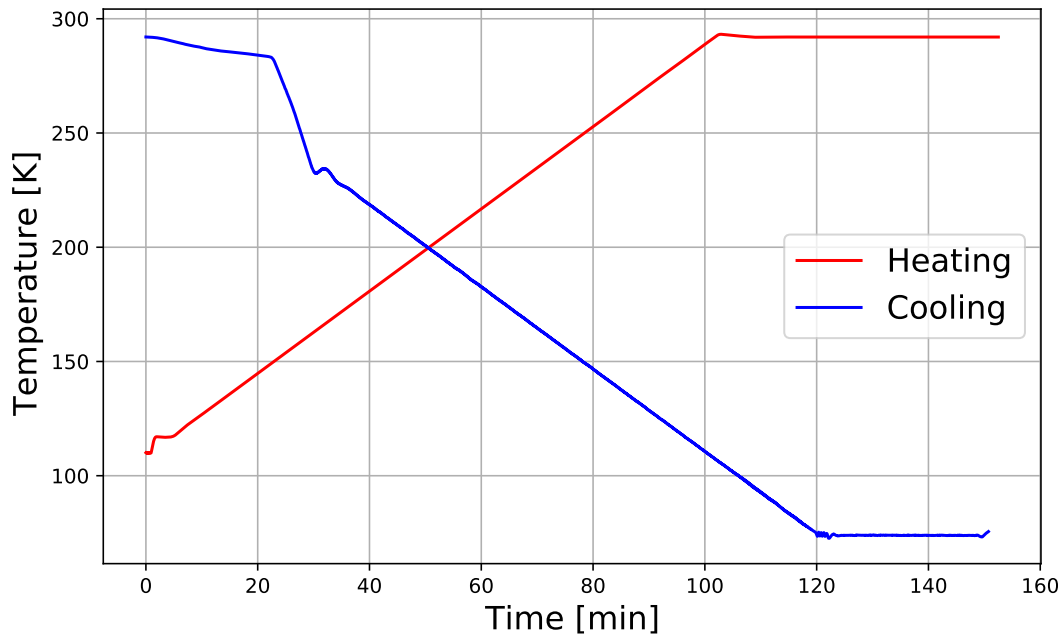


Figure 3.8: Cooling and heating cycles of the cryostat. A slope of 1 K can be seen for both the graphs.

To acquire the delay between thermalisation of in-built temperature sensor and our sample, we pumped the system with 756 nm light, and observed the transmission signal as the temperature was varied. The transmission was expected to change as the etalon length between the fibres would change from thermal expansion. Figure 3.9 shows that there was a few minutes of delay. So, new measurements at different temperatures were started 5-10 minutes after the cryostat stabilised.

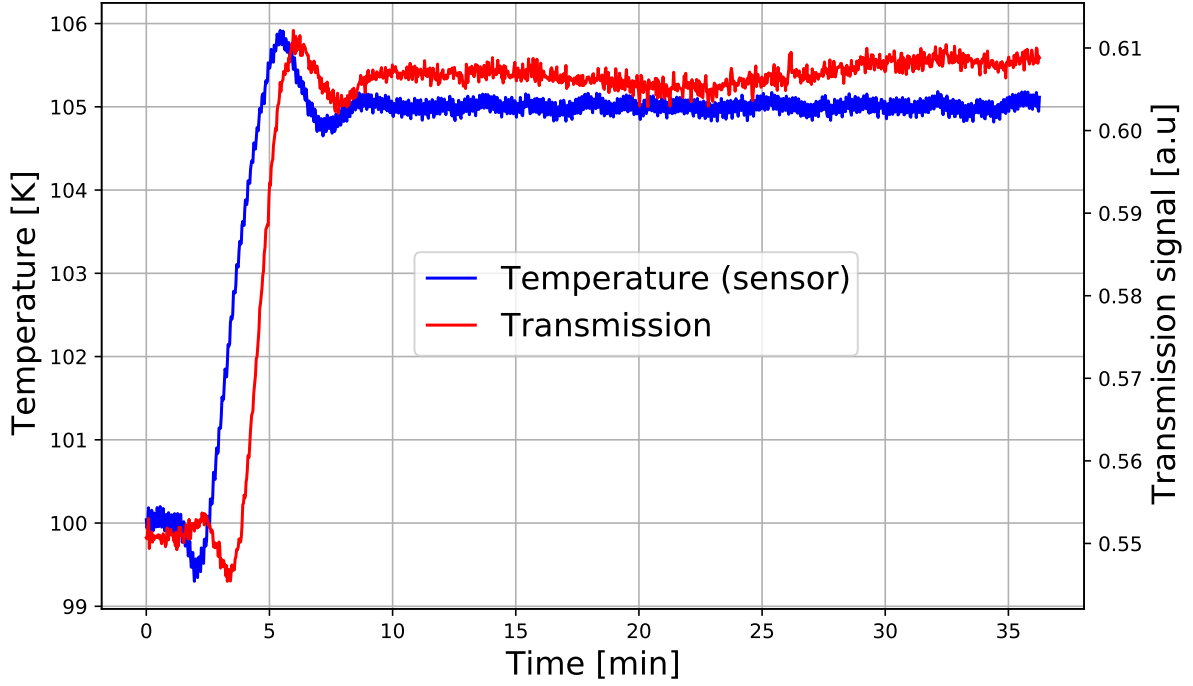


Figure 3.9: Change in transmission signal as temperature was changed. Observe a delay of about 2 min between the sample response and the temperature.

### 3.3.2 Spectroscopic results

With liquid nitrogen, we could reach a lowest temperature of 75 K. Above 80 K, PID feedback stabilised the cryostat within  $\pm 0.2$  K, hence we performed spectroscopic measurements from 80 K to 135 K, with increments of 5 K. Figure 3.10 shows the measured voltages from the three diodes at 80 K. Figure 3.11 shows the normalised signals at 80 K. The normalisation was performed using the relations 3.2. One can understand the importance of normalisation by comparing the two figures.

Following observations can be made by a visual inspection of the data acquired at 80 K:

- There is a drop in transmission around 754 nm.
- There is also a drop in reflection around 753 nm.
- The oscillation in transmission and reflection have a phase difference of  $\pi$ .

The phase shift between the reflection and transmission signals is expected, because if more light is transmitted, there will be a reduction in reflection, and vice versa. The dip in transmission can be attributed to the exciton resonance. But the dip in reflection however needs to be understood further.

To understand the phenomenon further, measurements were taken at various temperatures for comparison. To quantitatively analyse the signals, transmission data was fit with a function of the form 3.3:

$$T(\lambda) = \frac{(\lambda - \lambda_0)^2 + \left(\frac{\gamma'}{2}\right)^2}{(\lambda - \lambda_0)^2 + \left(\frac{\gamma + \gamma'}{2}\right)^2} + A \cos(2\pi f(\lambda - \phi)) + C \quad (3.3)$$

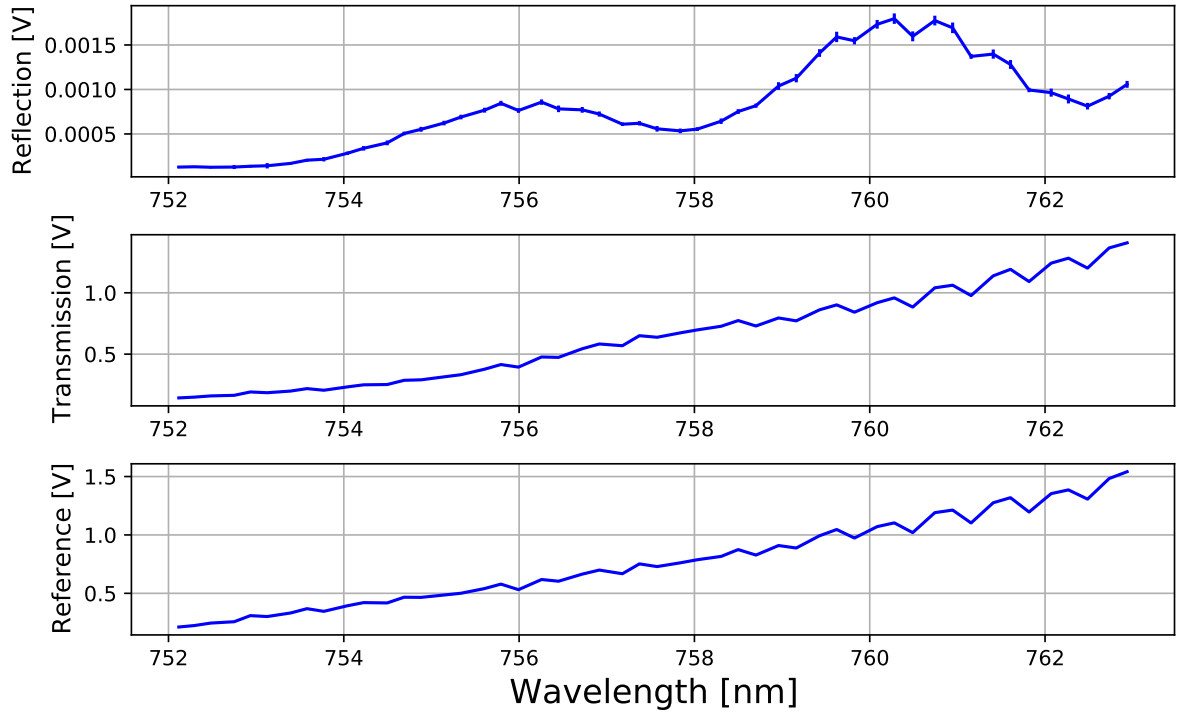


Figure 3.10: Voltage readings from the three diodes. Reference and transmission diodes were used with 50 dB gain and the reflection diode was used with 70 dB gain.

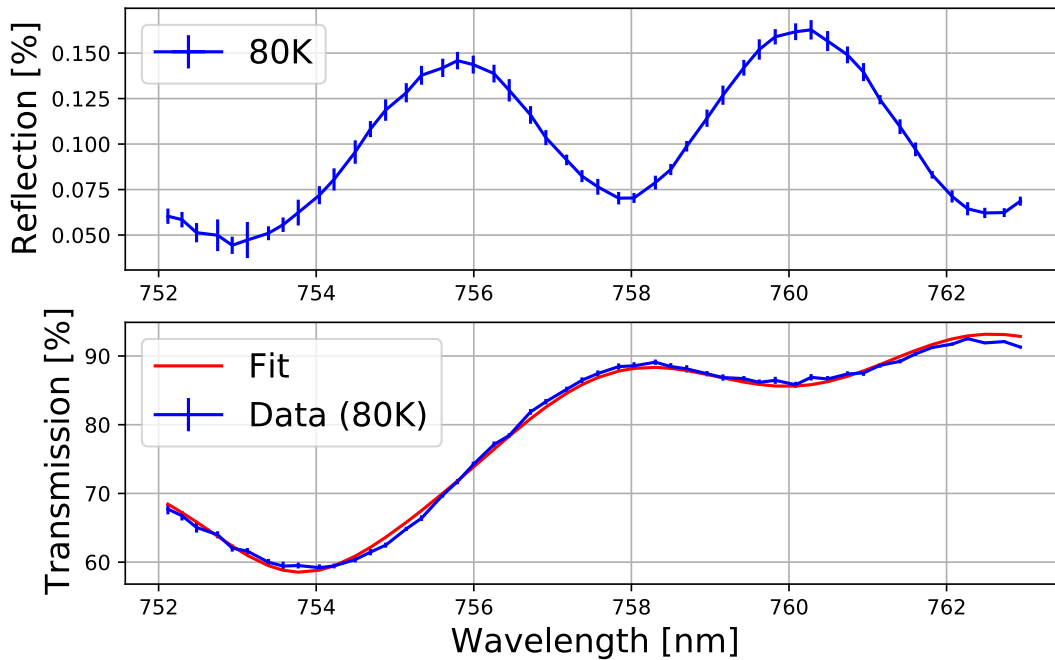


Figure 3.11: Normalised reflection and transmission signals. Normalisation performed using the relation 3.2. Equation 3.3 fitted to the transmission data is illustrated in the bottom figure.

with  $A$ ,  $C$ ,  $\lambda_0$ ,  $\gamma$ ,  $\gamma'$ ,  $f$ , and  $\phi$  being fit parameters. This can be compared with Equation 2.4 to obtain the location, strength and width of the resonance. An oscillatory term is added to compensate for the etalon effect, and an offset is added to compensate for other losses in the system (fibre coupling, etc.). Fit at 80 K is illustrated in Figure 3.11. Obtained parameters at

80 K is given in Table 3.1.

Parameter	Value
$\lambda_0$	753.6 nm
$\gamma$	0.8563 nm
$\gamma'$	3.4483 nm

Table 3.1: Obtained parameters for the resonance at 80 K. Obtained for transmission signal, as illustrated in Figure 3.11. The covariance matrix however couldn't be found due to the large number of fit parameters.

One can observe that the non-radiative line width is much larger than the radiative line width even at 80 K. Comparing these values with Figure 2.4, one can observe that the expected reflection power is very small. For the light reflected from the surface of the MM fibre, due to reduced transmission, the back coupling drops, leading to the reflection signal observed in Figure 3.11. To understand the resonance properties further, we repeated spectroscopic measurements at various temperatures. For clarity, the raw data at all temperatures is not illustrated in this thesis, but the Lorentzian from fits of transmission signals are illustrated in Figure 3.12.

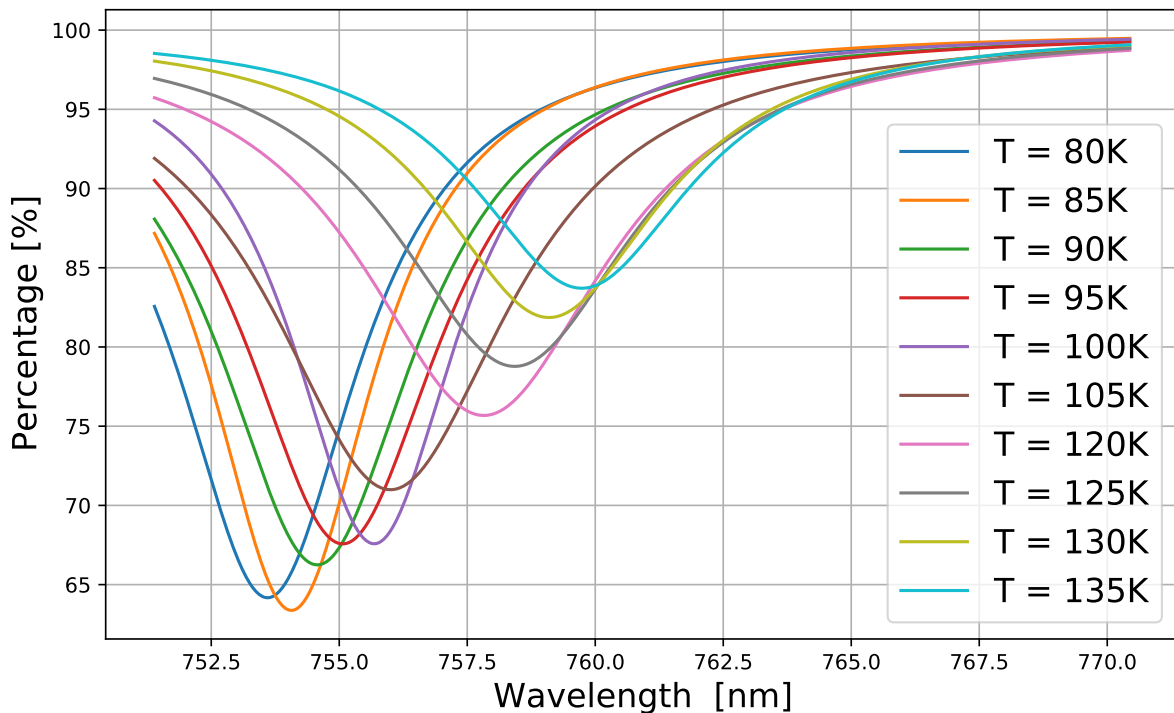


Figure 3.12: The first term from Equation 3.3 at various temperatures. One can observe the change in the resonance position, width and amplitude with temperature.

In Figure 3.12, one can clearly notice the shifts in resonance position, widths, and amplitudes. Change in resonance with temperature is graphically illustrated in Figure 3.13. Extracting  $\gamma$  and  $\gamma'$  from the data, Figure 3.14 illustrates the change in  $\eta$  (from 2.2) with temperature.

One can observe that the non-radiative line broadening is reduced as temperature is lowered. Thus, to have a larger  $\eta$ , we must cool down the sample further – say, by using liquid Helium.

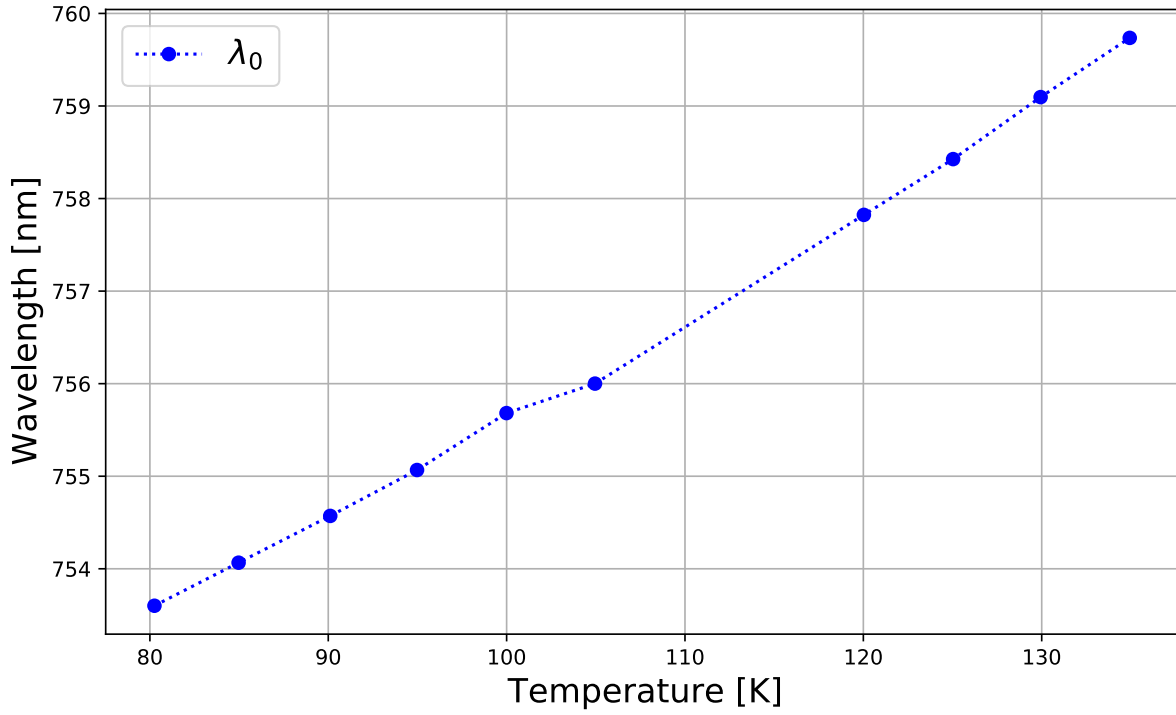


Figure 3.13: Variation of the resonance position ( $\lambda_0$ ) with temperature. Extrapolating from the graph, we expect the resonance to shift towards blue region as temperature is lowered further.

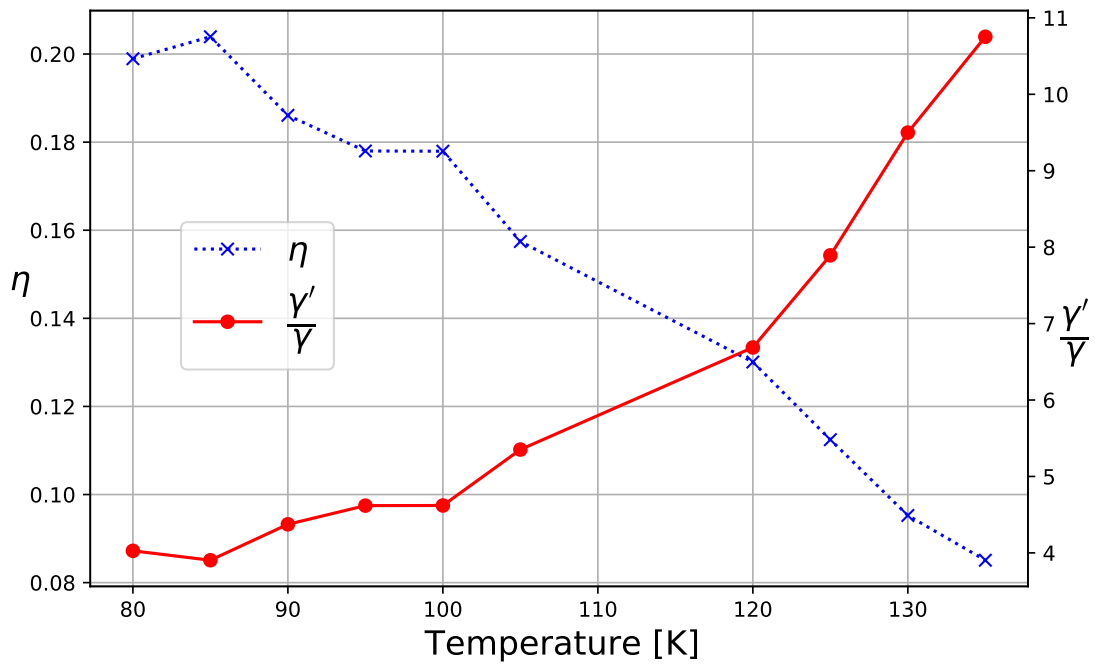


Figure 3.14: Variation of  $\eta$  and  $\gamma'$  (see 2.2) with temperature. Extrapolating from the graph, we expect  $\eta$  to increase as temperature is lowered further.

## Chapter 4

# Single-shot micro-fabrication

Parallely, we also had to work on the mirror fibre. To have a stable optical resonator, we need concave mirrors [35, 41, 17]. We have a CO<sub>2</sub> laser fabrication setup at our institute, jointly built by us and the group of Prof. Dr. Dieter Meschede <sup>1</sup> [42]. It was built based on the works of Hunger et al. [17]. It was used to fabricate concave structures onto the end facets of optical fibres. Structures with radius of curvature (ROC) from 150  $\mu\text{m}$  to 500  $\mu\text{m}$  with diameters from 20  $\mu\text{m}$  to 45  $\mu\text{m}$  were fabricated for various projects [14, 15, 16]. Meanwhile, there was research interest in obtaining structures with ROC from 800  $\mu\text{m}$  to 4000  $\mu\text{m}$ , with diameters from 75  $\mu\text{m}$  to 200  $\mu\text{m}$ . Thus, to reach these new regimes, and to broaden the capabilities of the previous setup, we had to understand the parameters in the experiment, and characterise the setup thoroughly.

In this chapter we consider fabrication by a single pulse of the laser – from here on termed as a “shot”. Changes made to the old experiment are described in section 4.1. Free parameters in the experiment are illustrated in section 4.2. A physical model is described in section 4.3 to understand the effects of these parameters, and section 4.4 presents the observational verification of the described model.

### 4.1 Setup

In the previous version of the experiment [43], the laser beam from CO<sub>2</sub> laser at a wavelength of 9.3  $\mu\text{m}$  was colimated using a 500mm lens, and expanded by 2x telescope. The beam power was controlled and stabilised using a Germanium acousto-optic modulator (AOM). The first order of the AOM was spatially filtered using a hollow capillary tube [44], and further by a pinhole. The capillary was made of fused silica and was internally coated with protected silver for guiding the beam. Polarisation was filtered using a thin film polariser (TFP) and was converted into a circularly polarised beam using a  $\lambda/4$  phase shifting plate. The beam was finally focussed using a 25 mm best form lens. All lenses in the experiment were made of anti-reflection (AR) coated ZnSe substrate, and all mirrors were gold coated optics. Figure 4.1 shows the current experiment with the changes made. The capillary and the pinhole are replaced in the current design, as explained in subsection 4.1.1.

#### 4.1.1 Spatial filtering

A drawback of the previous design was that any drifts in the beam coupling into the capillary would damage the in-coupling side of the tube, and any partial reflection from optics at the out-coupled side would damage the out-coupling side of the tube. Furthermore, the stainless steel pinhole was damaged over time, and its effectiveness was reduced. A robust and stable spatial filter had to be designed for this beam as a bad spatial profile in the beam would result

---

<sup>1</sup><http://quantum-technologies.iap.uni-bonn.de/>

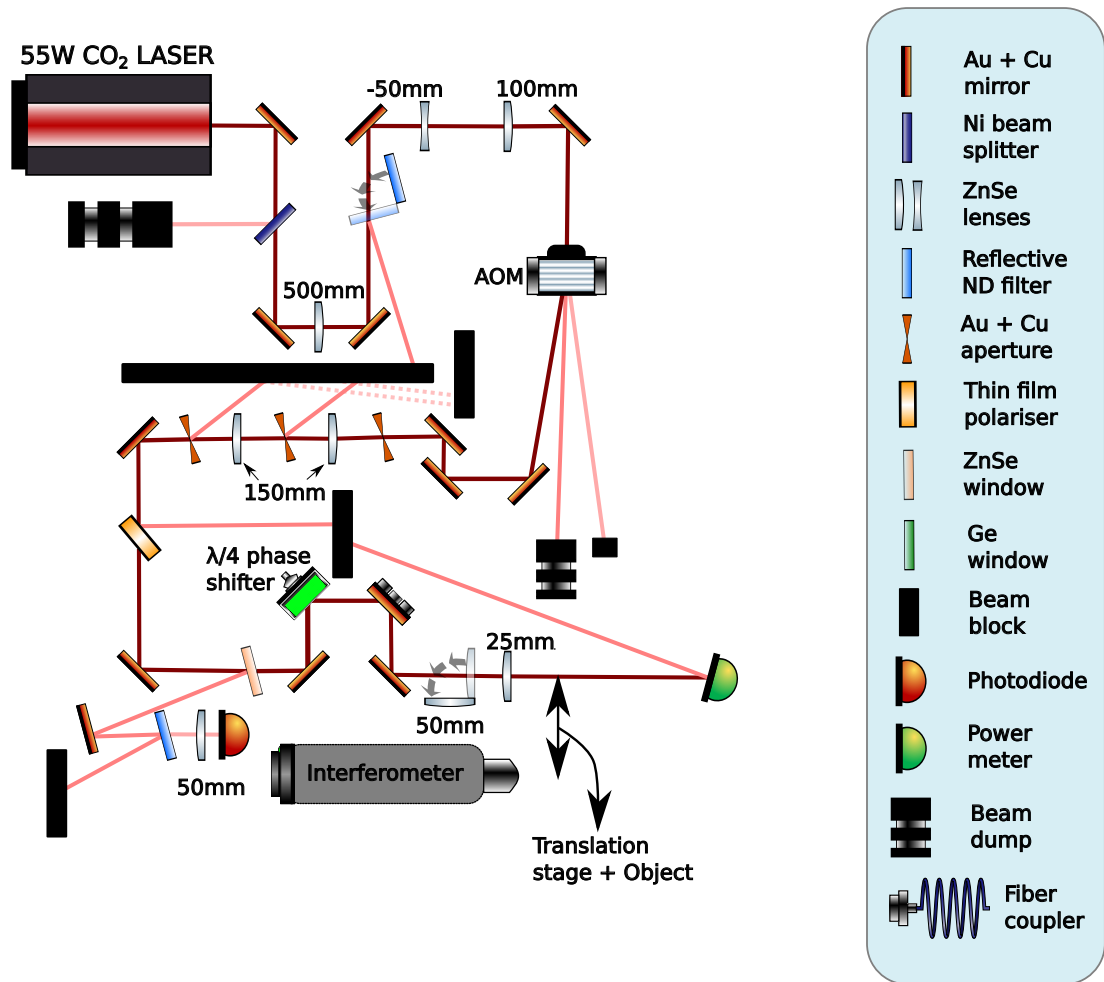


Figure 4.1: The new fibre shooting experiment.

in bad structures during fabrication.

Thus, we decided to use a commercial high power pinhole in combination with custom designed apertures for spatial filtering. We designed a  $4f$  configuration optical system as illustrated in Figure 4.2. 150 mm lenses were used for focussing the beam and for re-collimation. In this configuration, the image plane of the first lens would be a spatial Fourier transform of the object plane – which is the collimated beam in our case [35]. In this configuration, any circular aperture along the collimated beam would induce Airy-rings in the Fourier plane, which could then be clipped off efficiently using a pinhole of appropriate size. Any residual rings in the re-collimated beam could then be clipped efficiently using an iris. The collimated beam with a  $1/e^2$  waist of 2.2 mm was first filtered using a custom aperture of 6 mm, causing an Airy-like intensity distribution in the Fourier plane. Central spot of this pattern was then filtered out using a commercial high power pinhole<sup>2</sup> of diameter 500  $\mu\text{m}$ . The re-collimated beam had weak residual rings around a nice Gaussian intensity distribution, which were clipped using a stainless steel iris. Stainless steel could handle these low intensity rings well. The 6 mm aperture was however fabricated on a copper plate of 2 mm thickness, and was coated with around 120 nm gold at the research group of Prof. Dr. Stefan Linden at our institute. This acted as a reflective filter, thus reducing any possible damage by absorption. Any absorbed power would be dissipated efficiently by the copper substrate. 500  $\mu\text{m}$  pinhole was also a reflective one, thus reducing damages.

The new spatial filter removed about 60% of the input power, thus giving us around 5 W for

<sup>2</sup>Edmund optics 500  $\mu\text{m}$  Aperture Diameter, Gold-Plated Copper Aperture

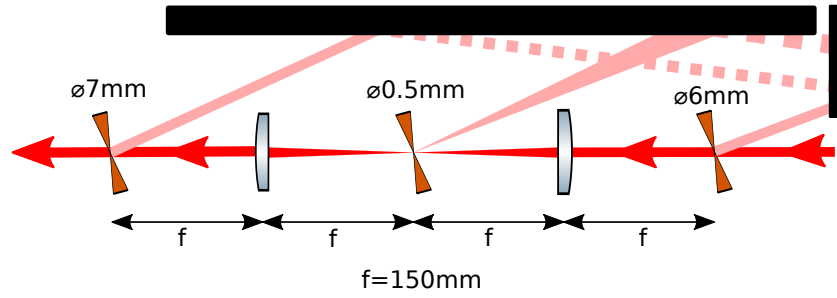


Figure 4.2: 4f configuration Fourier filter. The pinholes were tilted to pickup and block the reflections effectively.

fabrication purposes. To reduce further losses, we interchanged the 50-50 Beam splitter to a ZnSe pick-off plate for power stabilisation, as illustrated in Figure 4.1. To further improve the mode quality at the shooting position, we replaced the best form lens with an aspherical lens. With these changes, we had a superior beam with an ellipticity of less than 5% over 4 Rayleigh lengths, as shown in Figure 4.3. One can also notice a reduction in the new beam waist by a factor of 2 – which is necessary for fabricating smaller structures.

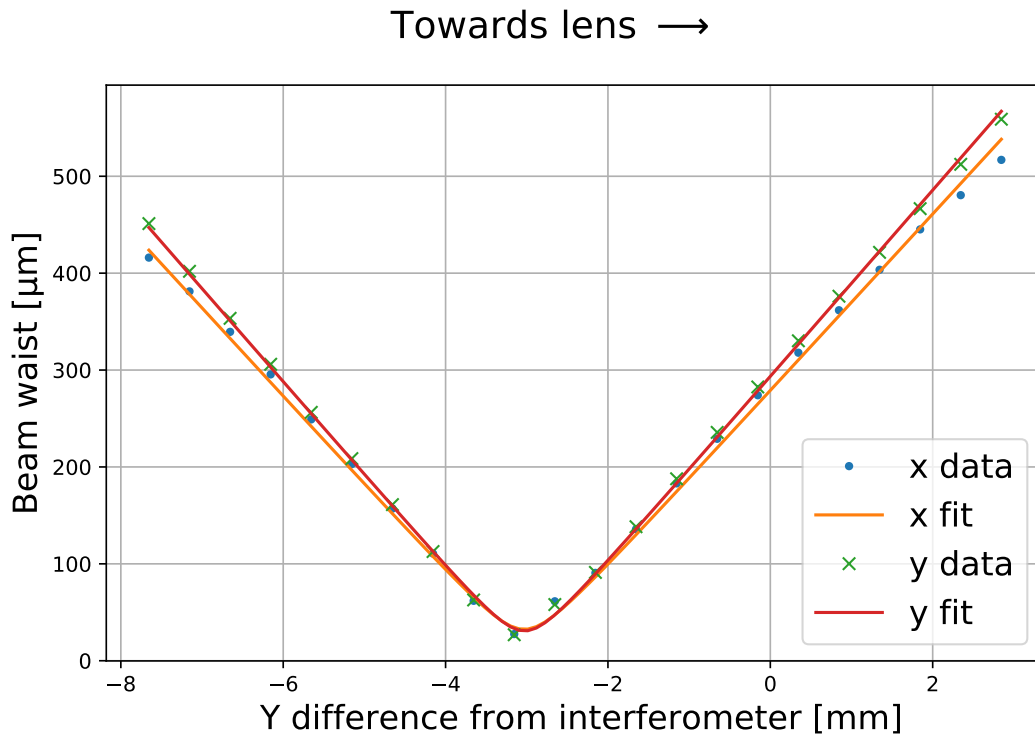


Figure 4.3: The new beam profile at shooting position with a beam waist of 31.1(5)  $\mu\text{m}$ . Measurement performed using a FLIR Boson IR camera.

## 4.2 Free shooting parameters

When using a Gaussian laser beam of given power and waist, one can use a multitude of parameters to control the resulting profile. Figure 4.4 illustrates the different parameters accessible, and Table 4.1 summarises the parameters and conventions used through out this thesis.

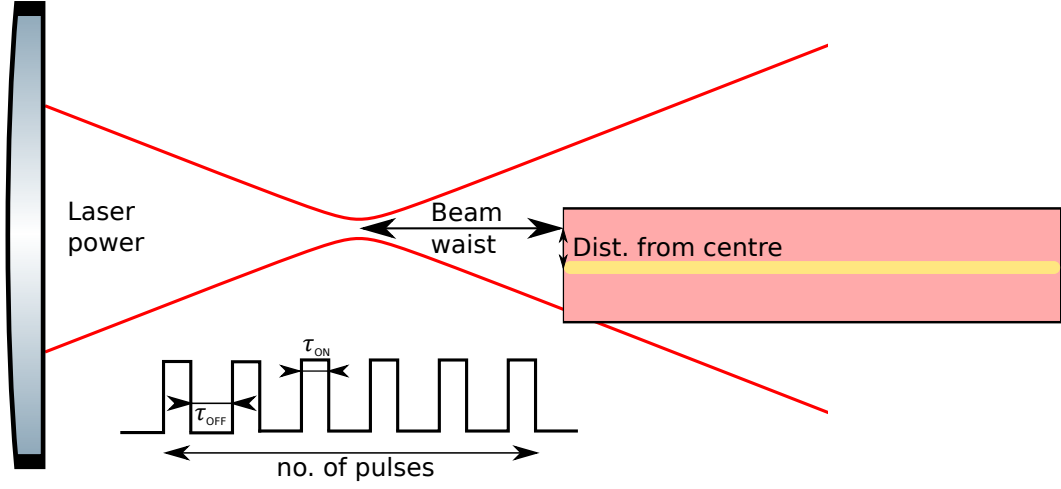


Figure 4.4: Free parameters in the CO<sub>2</sub> fibre shooting experiment.

Parameter	Range
Power (P)	(0.8 – 5) W
Pulse Duration ( $\tau_{ON}$ )	(0.05 – 5000) ms
Beam waist (a)	(30 – 4000) $\mu\text{m}$
No. of pulses (n)	integer
Delay bw. pulses ( $\tau_{OFF}$ )	(0.05 – 5000) ms
Dist. from centre ( $d_0$ )	(0 – 30) $\mu\text{m}$

Table 4.1: Free parameters in the experiment, and their respective regimes.

The laser beam power at the shooting position can be changed using the AOM, and the waist can be changed by moving the object along beam axis. The beam is pulsed using the AOM, and the pulse characteristics is controlled by modulating the AOM voltage with an appropriate waveform. For an optical fibre of given diameter, the offset of fibre axis with the beam axis is another parameter that can be controlled. This offset does not change the shot profile if the object boundary is far from the beam waist – as in the central region of a glass substrate.

In previous works [43, 45, 42], a “sweet spot” was found for power, beam waist, pulse duration, and the beam was centred at the optical fibre. The control of surface profile such as radius of curvature and depth was tuned by changing the number of pulses used. This limited the size of structures obtained, and the fixed values had to be found every time the setup was modified. Furthermore, we had to find various “sweet spots” for different regimes of radius of curvatures.

### 4.3 Modelling of laser ablation

To optimise the experiment further, and to make it universal, we had to understand the role each parameter played on the fabricated profile. The theoretical model from [46] is described below.

A CO<sub>2</sub> laser at 9.3 μm is used; it excites the vibrational energy levels of the SiO<sub>2</sub> molecules in glass and transfers energy. As the power used is in order of W, and the beam waist is in order of tens of μm, one can assume the most dominant energy transfer is thermal in nature [47].

Heat equation describing the flow of temperature  $T(\mathbf{r}, t)$  with a heat source  $S(\mathbf{r}, t)$  is given by Equation 4.1:

$$\frac{\partial T(\mathbf{r}, t)}{\partial t} = \frac{\kappa}{c_p \rho} \cdot \nabla^2 T(\mathbf{r}, t) + \frac{1}{c_p \rho} \cdot S(\mathbf{r}, t) \quad (4.1)$$

where  $\kappa$  is thermal conductivity,  $\rho$  is density of material, and  $c_p$  is specific heat capacity at constant pressure.

For a Gaussian beam of given waist, the intensity profile is given by:

$$I(\mathbf{r}, t) = I_0 I_t(t) e^{-\frac{r^2}{a^2}} \quad (4.2)$$

with  $r = \sqrt{x^2 + y^2}$ ,  $a$  being the 1/e waist,  $I_t(t)$  being the time dependent part, and  $I_0$  being the peak intensity. Everywhere else in this thesis, the mentioned beam waist is  $(1/r^2)$  radius, to be consistent with references.

Defining absorption fraction  $A$  as the fraction of input intensity absorbed by the material, and assuming the incident beam is the only source of heat for the material, one gets:

$$S(\mathbf{r}, t) = A \cdot I_0 I_t(t) e^{-\frac{r^2}{a^2}} \quad (4.3)$$

as the heat source in the problem. Complex refractive index for a standard optical glass such as fused silica at  $\lambda = 9.3 \mu\text{m}$  is  $n \approx 2.3 + 2i$  [48]. Using the relation 4.4

$$\alpha = \frac{4\pi \cdot \Im(n)}{\lambda} \quad (4.4)$$

for absorption coefficient [31], one finds the penetration depth to be 370 nm. Since this is much smaller than typical depth of structures obtained, one can assume the heat source to be only at surface of the material. Comparing above calculation for other CO<sub>2</sub> lasers at  $\lambda = 10.6 \mu\text{m}$  gives a complex refractive index of about  $2.3 + 0.2i$  and a penetration depth of  $3.7 \mu\text{m}$ . This is in the same order of magnitude as structure depth, hence the model developed here might not be accurate. Considering the heat source is only on the surface, inserting 4.3 into 4.1, and rewriting Equation 4.1 in integral form, one obtains:

$$T(\mathbf{r}, t) = \frac{A I_0 a^2}{D} \cdot \sqrt{\frac{\kappa}{\pi}} \cdot \int_0^t dt' \frac{I_t(t-t')}{\sqrt{t'(a^2 + 4Dt')}} e^{-\frac{r^2}{a^2 + 4Dt'}} \quad (4.5)$$

where  $D = \frac{\kappa}{c_p \rho}$ . In order to derive this, following approximations were made:

1.  $\kappa, \rho, c_p$  do not depend on temperature.
2. The boundary of object is very far from the beam, so spatial integral is performed in full space.
3. Heat flow along axial direction is minimal.

Approximation 1 is made to simplify the calculation. Approximations 2 and 3 are valid for shots done near the centre of a large object such as a glass substrate.

As most of ablation happen around  $r = 0$ , taking terms up to second order in  $r$  from Taylor expansion of Gaussian 4.6:

$$e^{-\frac{r^2}{a^2}} \approx 1 - \frac{r^2}{a^2} + o(r^4) + \dots \quad (4.6)$$

and having a temporal pulse of duration  $\tau$  gives Equation 4.7:

$$T(\mathbf{r}, t) = \frac{AI_0a^2}{D} \cdot \sqrt{\frac{\kappa}{\pi}} \cdot \int_0^\tau dt' \frac{\left(1 - \frac{r^2}{a^2 + 4Dt'}\right)}{\sqrt{t'}(a^2 + 4Dt')} \quad (4.7)$$

This integral can be solved to get:

$$T(\mathbf{r}, t) = \frac{AI_0a^2}{D} \cdot \sqrt{\frac{\kappa}{\pi}} \cdot \frac{1}{a^3} \left[ \frac{(2a^2 - r^2)}{\sqrt{D}} \cdot \tan^{-1} \left( \sqrt{\frac{\tau}{\left(\frac{a^2}{4D}\right)}} \right) - \frac{2ar^2\sqrt{\tau}}{a^2 + 4D\tau} \right] \quad (4.8)$$

This gives the temperature distribution on surface after the pulse is incident. The time scale of the problem is given by:

$$\tau_0 = \frac{a^2}{4D} \quad (4.9)$$

For fused silica  $\kappa = 1.38$ ,  $\rho = 2203 \text{ kg m}^{-3}$ ,  $C_p = 1850 \text{ J kg}^{-1} \text{ K}$ , one finds  $\tau_0 = 1.38 \text{ ns}$ . Thus, for  $\tau \gg \tau_0$ , steady state temperature is given by Equation 4.10:

$$T_s(\mathbf{r}, t) = \frac{AP}{2aD^{\frac{3}{2}}} \cdot \sqrt{\frac{\kappa}{\pi}} \cdot \left(1 - \frac{r^2}{2a^2}\right) \quad (4.10)$$

where we have defined  $P = I_0 \cdot \pi a^2 / 2$  as the power of the laser beam. Ablation can be modelled by [49]:

$$v = v_0 e^{\frac{-U}{k_B T}} \quad (4.11)$$

where  $v$  is the velocity of material removal (velocity of ablation front),  $v_0$  and  $U$  being object constants. From this, one can get the ablated profile by integrating over time:

$$D(x, y) = \int v_0 e^{\frac{-U}{k_B T}} dt \quad (4.12)$$

For steady state, one can show

$$D(x, y) \approx \tau \cdot v_0 e^{\frac{-U}{k_B T_s}} \quad (4.13)$$

Substituting Equation 4.10 into Equation 4.13, one gets:

$$D(r) \approx \tau \cdot v_0 e^{\left[ \frac{-U}{k_B} \cdot \frac{2aD^{\frac{3}{2}}}{A \cdot P} \cdot \sqrt{\frac{\pi}{\kappa}} \cdot \frac{1}{1 - \frac{r^2}{2a^2}} \right]} \quad (4.14)$$

at  $r = 0$ , one finds

$$D_0 = \tau \cdot v_0 e^{\left[ \frac{-2aUD^{\frac{3}{2}}}{A \cdot P \cdot k_B} \cdot \sqrt{\frac{\pi}{\kappa}} \right]} \quad (4.15)$$

which is the depth of ablated structures.

From these results, following observations can be made:

- Depth of shot structure increases linearly with pulse duration  $\tau$  and drops exponentially with increasing beam waist.
- Structure width increases with power and beam waist.
- A saturation effect for depth is seen as power is increased while keeping all other parameters constant.
- The size of structures change as a function of  $P/a$ .

## 4.4 Experimental verification of the model

As a first step, we used fused silica glass substrates<sup>3</sup>. With a beam waist in order of tens of  $\mu\text{m}$ , a 25 mm diameter substrate had no effect on the shots in central 20 mm region owing to its large boundary. Furthermore, using a single substrate made the preparation and alignment process faster. To reduce the large parameter space, the beam waist was kept constant at around 70  $\mu\text{m}$ .

We varied the power from 0.9 W to 3.5 W to test the above model. For each given power, shots were done at different pulse durations. Obtained characteristics is illustrated in Figure 4.5.

One can observe the linear relationship between the depth of structures and pulse duration at all the laser powers used. Relation 4.15 with an offset was fit to our data in a 3 dimensional power – pulse duration – depth hyperspace and is also illustrated in the figure. An offset was added to Equation 4.15 as a compensation for the assumptions we made. From Equation 4.15,  $A$ ,  $v_0$ , and the offset were kept as free parameters for fitting. Obtained values are presented in Table 4.2.

Parameter	Value
$v_0$	0.022 40(81) $\text{m s}^{-1}$
$A$	1.543(5)
offset	-2.09(11) $\mu\text{m}$
RMS error	242.69 nm
$r^2$ value	0.9513

Table 4.2: Fit parameters for  $\text{CO}_2$  laser ablation on fused silica substrate.

Similar experiment was also confirmed with optical fibres. With the large  $r^2$  value, we can conclude that our model for depth is good. One observes the absorption fraction  $A$  to be greater than 1, and this can be attributed to the fact that we used approximate values for  $U = 3.6 \text{ eV}$ ,  $\kappa = 1.38 \text{ W m}^{-1} \text{ K}^{-1}$ , and  $C_p = 1850 \text{ J K}^{-1} \text{ kg}^{-1}$ .

Thus, using this model, one can form a basis of shots as a starting point for laser-dot milling, and other complex processes. With the small beam waist, we obtained structures with ROC upto 45  $\mu\text{m}$  on the lower side. By increasing the power and beam waist, we obtained structures with diameter up to 150  $\mu\text{m}$  on the substrate. To fabricate even larger structures using single shots, we need more power!

---

<sup>3</sup>Thorlabs WG41050

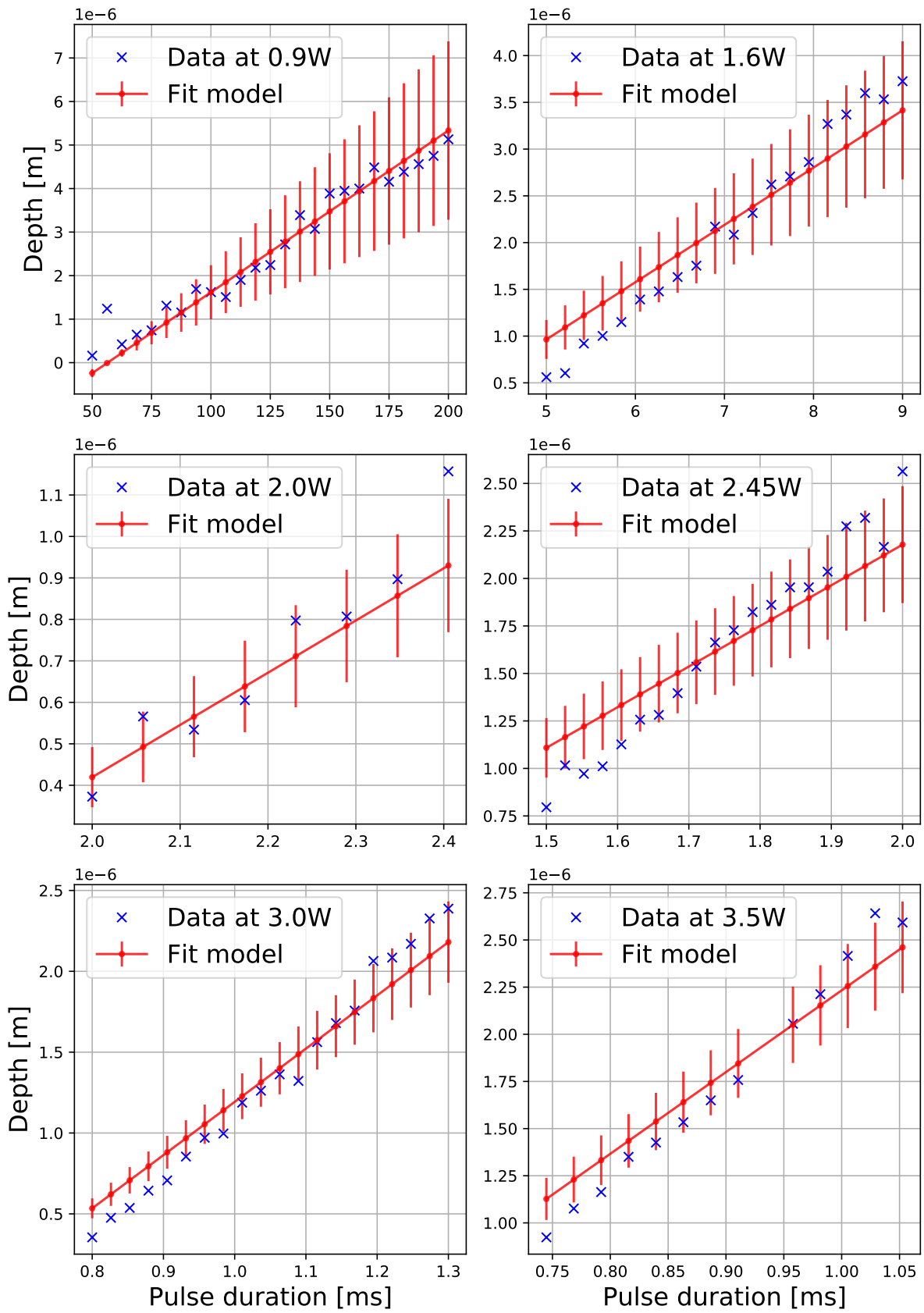


Figure 4.5: Variation of depth with pulse duration. The fit was performed in a power – pulse duration – depth hyperspace. The error bars were generated considering 3% power fluctuations.

# Chapter 5

## Multi-shot micro-fabrication

It is shown in chapter 4 that one can obtain structures of radius of curvature from  $45\ \mu\text{m}$  onwards using single-shots by changing different shot parameters described in section 4.2. But if one increases the beam diameter on an optical fibre, the fibre edge starts to melt at certain point, which sets a limit on the structure diameter obtained using single-shot technique. In order to fabricate larger structures, or to polish a macroscopic optical element, one has to perform laser dot-milling with multiple shots. To fabricate structures that do not have a Gaussian profile, or to change the ellipticity of single-shot structure, multi-shot technique must be used.

In this chapter, simple applications of multi-shot technique are discussed in section 5.1. Non-linearity of laser dot-milling is presented in section 5.2, the new experimental control software using python is described in subsection 5.3.2, and further improvements made on the setup are described in subsection 5.3.1.

### 5.1 Simple application of multiple shots

When one uses more than a single laser pulse, a new parameter that has to be taken into account, is the delay between independent pulses. In order to understand the typical timescale of cooling of an optical fibre and a substrate, 5 pulses were shot with varying delay between them. Figure 5.1 illustrates the observations. Fitting an exponential decay function to the data, one obtains a time constant of  $57.13\ \text{ms}$  for an optical fibre and  $0.73\ \text{ms}$  for a fused silica substrate. A difference of two orders of magnitude can be explained by the fact that heat can dissipate faster through a large substrate when compared to an optical fibre. Thus, all further multi-shot trials were done with delay between the pulses of about  $2\ \text{s}$ , which is much larger than the obtained time constants. This should make subsequent pulses independent from each other.

#### 5.1.1 Ellipticity control

When we use the concave structures in high finesse optical resonators, ellipticity in the shots can result in polarisation mode splitting [50]. Some applications require perfectly symmetric shots, and some specific ellipticity. An immediate need for our group was to have perfect symmetric shots on an optical fibre. In order to control this, the minor axis of the profile from a single shot was obtained, and few displaced shots along the minor axis were made to compensate for the ellipticity. To reduce the 5% ellipticity we observed, we displaced some shots by  $\pm 5\ \mu\text{m}$  for compensation.

#### 5.1.2 Laser polishing

When one wants to build very high finesse optical resonators, the finesse is given by Equation 5.1 [35, 41]:

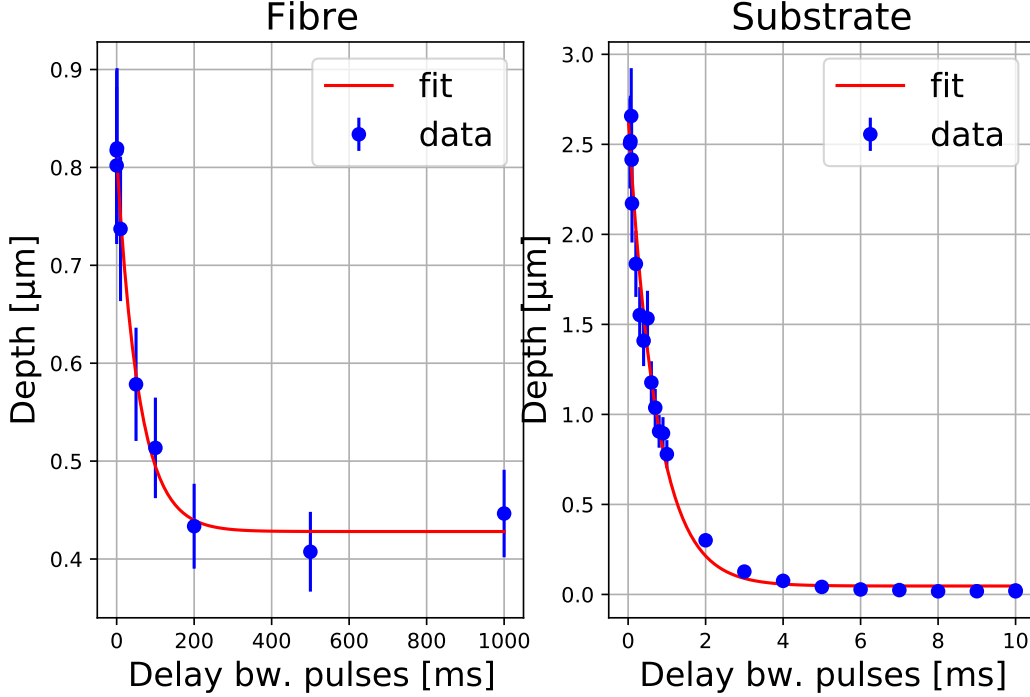


Figure 5.1: Effect of delay between pulses. Observe the difference in cooling time for the two. Uncertainty of about 10% in our outcome is also illustrated.

$$\mathcal{F} \approx \frac{2\pi}{T + \text{Losses}} \quad (5.1)$$

where  $T$  is total transmittance of resonator mirrors. Finesse is a measure of quality of optical resonators, and loosely describes the number of round trips a photon undergoes before leaving the resonator. Further details on optical resonators can be found in [35]. There is a strong research interest in our group to build optical resonators of length in order of few mm with finesse of about  $5 \times 10^4$ . As described in Equation 5.1, every loss channel for photons contribute strongly for drop in finesse. Following are some important loss channels:

- Absorption losses in the reflective coating. This can only be reduced by using different materials for coating, and hence can be used as a fundamental limit for finesse.
- Clipping losses from the edges of mirror. As light takes multiple round trips in the resonator, if the mirrors are not large enough, the photons can escape at the edges over time – reducing finesse. In order to reduce this effect, one has to have larger mirrors. To fabricate larger structures with given  $\text{CO}_2$  laser power, one has to do laser dot-milling. This will be described in subsection 5.2.3.
- Alignment losses. If the resonator is not aligned well, photons can escape from them over time, reducing finesse. To reduce the sensitivity of alignment, one can change the radius of curvature of the resonator mirrors as described in [41, 51]. The trivial solution to this problem is however to perform better alignment.
- Scattering losses from the substrate. If the substrate is not polished well enough, light can scatter off defects. Defects here include scratches, high-frequency roughness, and astigmatism. To obtain very low scattering losses, one needs super-polished mirrors, which are very expensive. Thus, we attempted to polish optics using our  $\text{CO}_2$  laser. This has been done before in [52].

As described in chapter 4, assuming the ablation process is mostly thermal in nature, if we heat the substrate using our laser beam just enough to melt the glass, but not enough to evaporate material, the molten surface becomes smooth due to surface tension and quickly solidifies. This must result in extremely smooth surfaces at an atomic level! The scratch-dig roughness can however only be measured using powerful techniques such as with an atomic force microscope (AFM). Since we do not have an AFM at our research group, a thorough characterisation of laser polishing is currently undertaken by another student from our group in collaboration with a different institute.

## 5.2 Non-linearity of multiple shots

Laser polishing may remove high frequency roughness and scratches. But in order to reduce clipping losses and astigmatism, one needs larger mirrors with better surface profile. Mirror sizes can be increased by using larger beam waist, but one must also increase the laser power proportionately according to Equation 4.15. Since we have a limit on laser power, other avenues must be explored to fabricate larger structures. One way to do this is by using multiple displaced shots, in contrast to single or concentric shots. Before approaching this problem, one must explore some non-linearities involved.

### 5.2.1 Off-centre shots

When one is fabricating on optical fibres, the boundary of fibre can interfere with lateral heat flow, and can cause deviations in our model from chapter 4. The dependence of depth on centering of the shots on a fibre is illustrated in Figure 5.2. This was done on SM fibre<sup>1</sup> with 5  $\mu\text{m}$  core diameter.

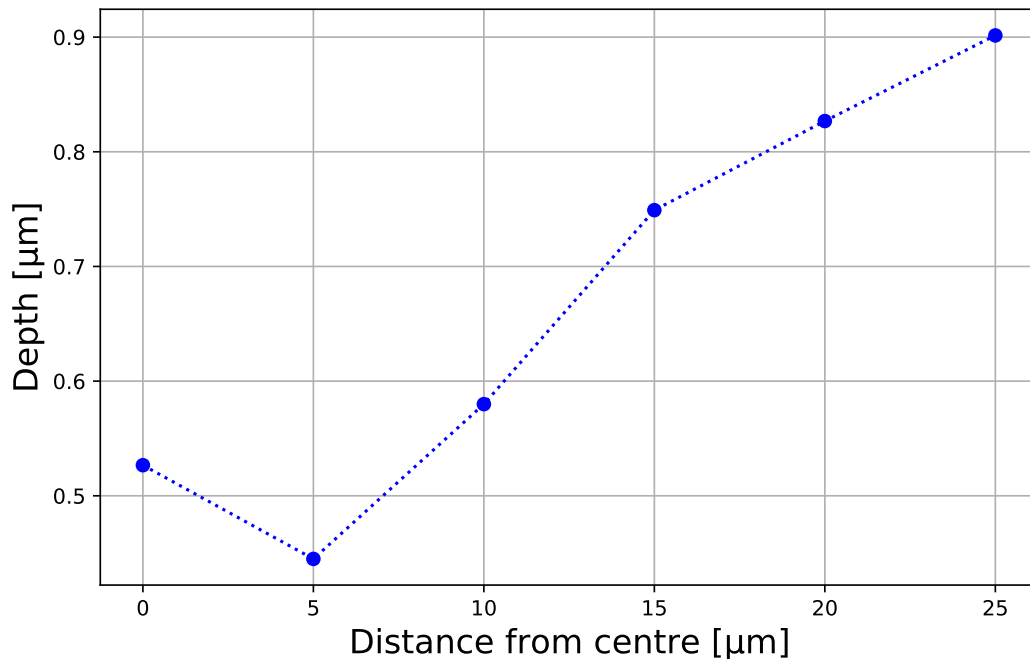


Figure 5.2: Effect of off-centre shots on a SM fibre of core diameter 5  $\mu\text{m}$  and cladding diameter 125  $\mu\text{m}$ .

One observes a drop in depth for shots performed 5  $\mu\text{m}$  away from centre. This can be attributed

---

<sup>1</sup>Thorlabs 780HP

to the core of SM fibre. Thus, one must compensate for the off-centre effects while attempting to perform laser dot-milling on an optical fibre.

### 5.2.2 Superimposed shots

The simplest multi-shot technique has already been described in previous works. In this case, concentric shots are done to control the radius of curvature. However, a more useful quantity is the depth of obtained structure. When we plot depth vs. number of laser pulses in Figure 5.3, one clearly observes a non linear relationship between the two. This hints to the complexity of heat flow and the ablation process. Similar behaviour was observed at different parameter regimes too.

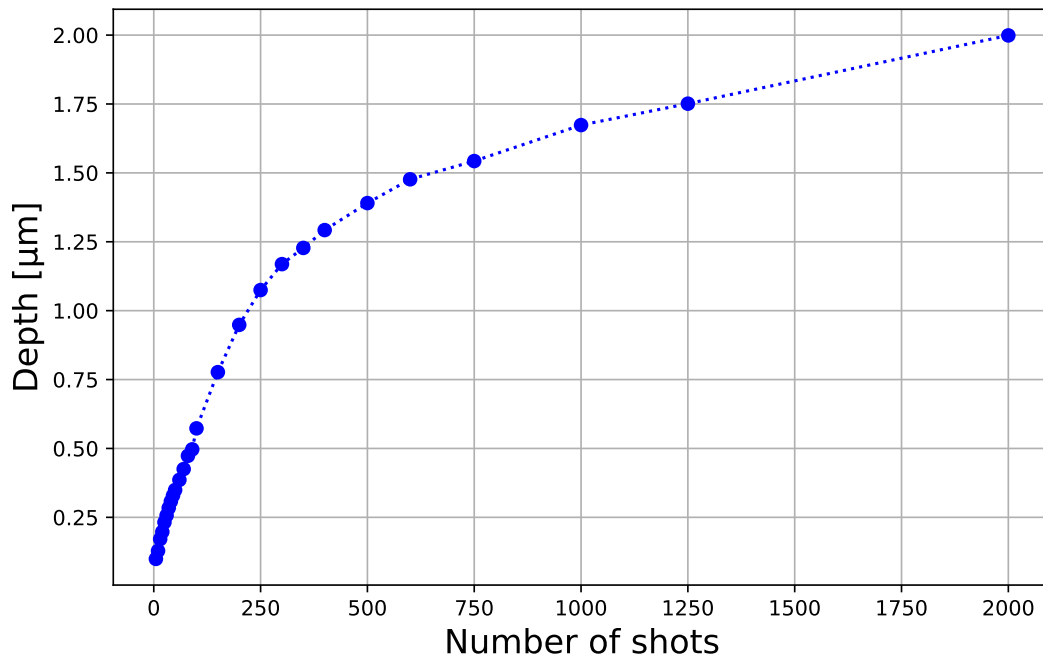


Figure 5.3: Non linearity in superimposed shots at 800 mW. Similar square-root behaviour was observed at different powers, even for small number of shots. Data acquired with a SM fibre.

### 5.2.3 Displaced shots – laser dot milling

To understand the non-linearity of displaced shots, we made rings of shots, but changed shot order. Appendix B illustrates the shot order, and their corresponding results. In an ideal case, the ring should look the same irrespective of the order in which shots were done. But we observed different results for different shot order. Furthermore, the obtained patterns were reproducible only within 90%.

Multiple factors can contribute to this:

- Change in angle of incidence for the laser beam after previous shots are done. After each shot, the new surface has local variation in slope. From Fresnel equations [35], we know that transmitted power, and hence absorption fraction  $A$  changes with angle of incidence.
- Change in absorption fraction  $A$  due to change in refractive index. As glass melts and solidifies after each shot, there can be a change in refractive index.
- Minute variation in the substrate. Local stress in the glass can contribute to uneven refractive index for the laser.

Fresnel equations for transmission coefficient is given by Equation 5.2

$$t_S(\theta_i, \theta_r) = \frac{2n_1 \cos(\theta_i)}{n_1 \cos(\theta_i) + n_2 \cos(\theta_r)} \quad \text{and} \quad t_P(\theta_i, \theta_r) = \frac{2n_1 \cos(\theta_i)}{n_2 \cos(\theta_i) + n_1 \cos(\theta_r)} \quad (5.2)$$

where  $t_S$  and  $t_P$  are transmission coefficients for S and P polarisations.  $\theta_i$ , and  $\theta_r$  are incidence and refraction angles, and  $n_1$  and  $n_2$  are complex refractive indices for vacuum and glass in our case ( $n_2 \approx 2.3 + 2i$  [48]). Transmitted power is given by the absolute square of transmission coefficients. Transmitted powers for S, P and circularly polarised light are plotted in Figure 5.4. One can observe that transmission is not very sensitive for circular polarisation up to about  $40^\circ$ , hence usage of  $\lambda/4$  phase plate in our experiment is justified.

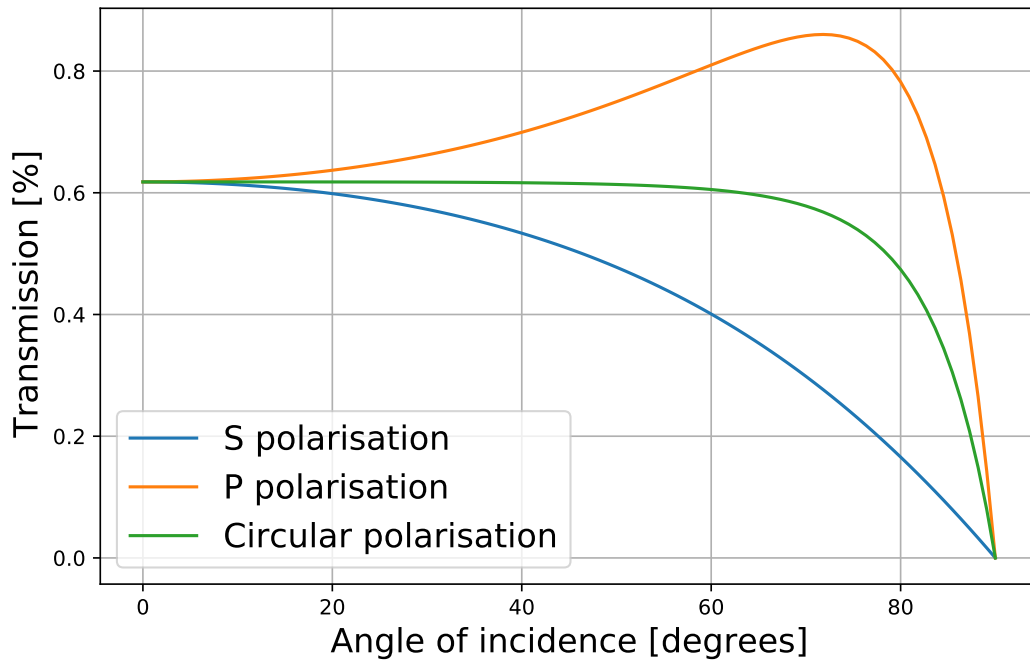


Figure 5.4: Transmitted power for S, P and circular polarisations for  $n_1 = 1$  and  $n_2 = 2.3 + 2i$  using Equation 5.2.

Observing the figures in Appendix B, one can feel the effect shot pattern has on the resulting profile. I hypothesised that effect of current shot depends on the previous profile in a linear fashion. This can mathematically be represented as Equation 5.3:

$$S_{N+1}(x, y) = S_N(x, y) + SP_{N+1}(x, y) \cdot (\alpha + \beta \cdot S_N(x, y)) \quad (5.3)$$

where  $S_N(x, y)$  is the surface profile after  $N^{\text{th}}$  shot,  $SP_N(x, y)$  the  $N^{\text{th}}$  single shot profile on bare substrate, and  $\alpha$  and  $\beta$  being some constants. With this model, when  $\alpha = 1, \beta = 0$ , one retrieves a simple linear relationship. Appendix B also illustrates the above model for each of the pattern with  $\alpha = 1, \beta = 250$ . One can notice some visual similarity between the data, and the model. Unfortunately, fitting the model with data did not result in same  $\alpha$  and  $\beta$  for different shot patterns. Thus, we concluded that ultra precise laser dot-milling is very non linear, and is difficult to predict with the required precision.

### 5.3 Towards complete automation

Summing up, following challenges still stood with the experiment:

- Any beam drifts had to be corrected using a feedback mechanism.
- With better understanding of single shots in chapter 4, we had new degrees of freedom to utilize in the experiment, but an algorithm had to be developed for selection of different parameters for specific applications.
- Ellipticity control and laser polishing were important tools offered by the experiment, but the parameters for these processes had to be calculated manually by the users for their specific needs.
- Laser dot-milling was not reproducible with required precision. An active feedback mechanism had to be developed, which could tweak the experimental parameters on the fly.

### 5.3.1 Final setup with additional updates

#### The new interferometer scheme

Appendix A describes the sequence of steps performed to fabricate one structure. The slowest step is the process of surface reconstruction using the white interferometer. With a spectral line width of about 300 nm, we have a coherence length of about  $2\ \mu\text{m}$  [35]. Though this allows us to position our substrate or fibre within an uncertainty of coherence length, the reconstruction is slow. One must scan the interferometer objective by more than the depth of our structures to successfully reconstruct the entire surface [42, 43]. This includes few hundred scan steps, increasing the time for reconstruction (in order of minutes). A narrow light source can however be used to speed up the process [53], but would result in loss of precision in placement of the object owing to its large coherence length. Thus, we decided to include both light sources in a switchable fashion. An electric relay as digital switch was used for this purpose. The new interferometer illumination scheme is illustrated in Figure 5.5.

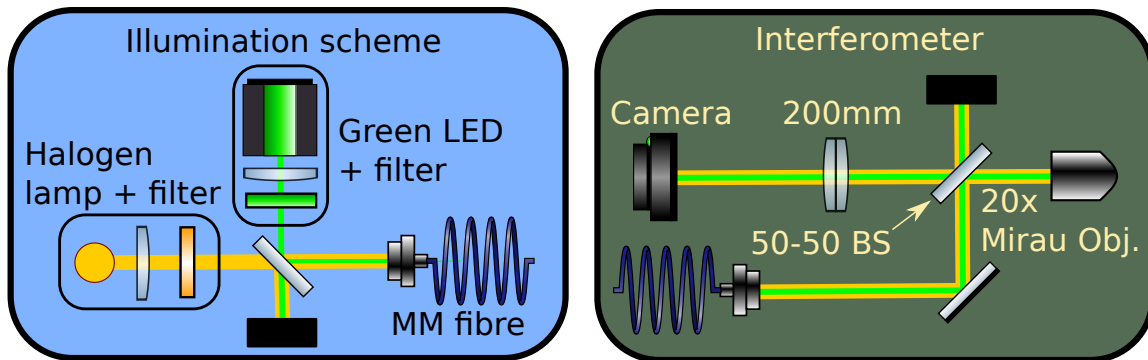


Figure 5.5: The new interferometer. A green LED and a halogen lamp are used in a switchable fashion. Large core MM fibre is used to transfer light from the sources to the interferometer.

A halogen lamp with a visible band pass filter was used to spectrally shape the light into a Gaussian profile. Parallely, a green LED with a line pass filter at 532 nm and line width 1 nm was added. The two light sources were mixed using a 50-50 beam splitter and were coupled into a large core multi-mode (MM) fibre. The collimated light from the fibre was used in interferometer. The next step is to include the algorithm for narrow light source for faster surface reconstruction.

## Visible lasers overlay

Typically, beam drifts are detected using quadrant diodes, and are compensated using motorised mirror mounts and a feedback loop. Quadrant diodes that are sensitive at wavelength  $9.3\mu\text{m}$  are expensive. Furthermore, since the final shooting lens is illuminated only during shooting, active stabilisation of beam is difficult. If one assumes beam drifts are caused by thermal effects on optical elements, the effect must be common for beams of any wavelength. Thus, we decided to superimpose the  $\text{CO}_2$  (IR) laser with a visible laser.  $\text{ZnSe}$  optics and gold coated mirrors are also effective for visible light, making the overlay useful. Anti reflection (AR) coated Ge windows are transparent for the IR beam, but reflects visible light strongly, hence we used these as dichroic mirrors for the overlay process. Two green laser pointers were used for this purpose. They were collimated using SM fibres and overlaid with the IR beam as illustrated in Figure 5.6. The thin film polariser reflected most of the visible light, hence we used a second beam after it. We selected the Germanium crystal of the AOM as the point of superimposition. Since the AOM is operated in Raman-Nath regime [35], the visible beam had to incident on AOM through its 0<sup>th</sup> order, so it is reflected onto the 1<sup>st</sup> order. Since an AR coated Ge window reflects about 1% of IR, the back reflected beam from the window can damage the fibre coupler of green laser. Hence two Ge windows were used, so only 0.01% of IR radiation would be reflected. This had negligible affect on the fibre coupler.

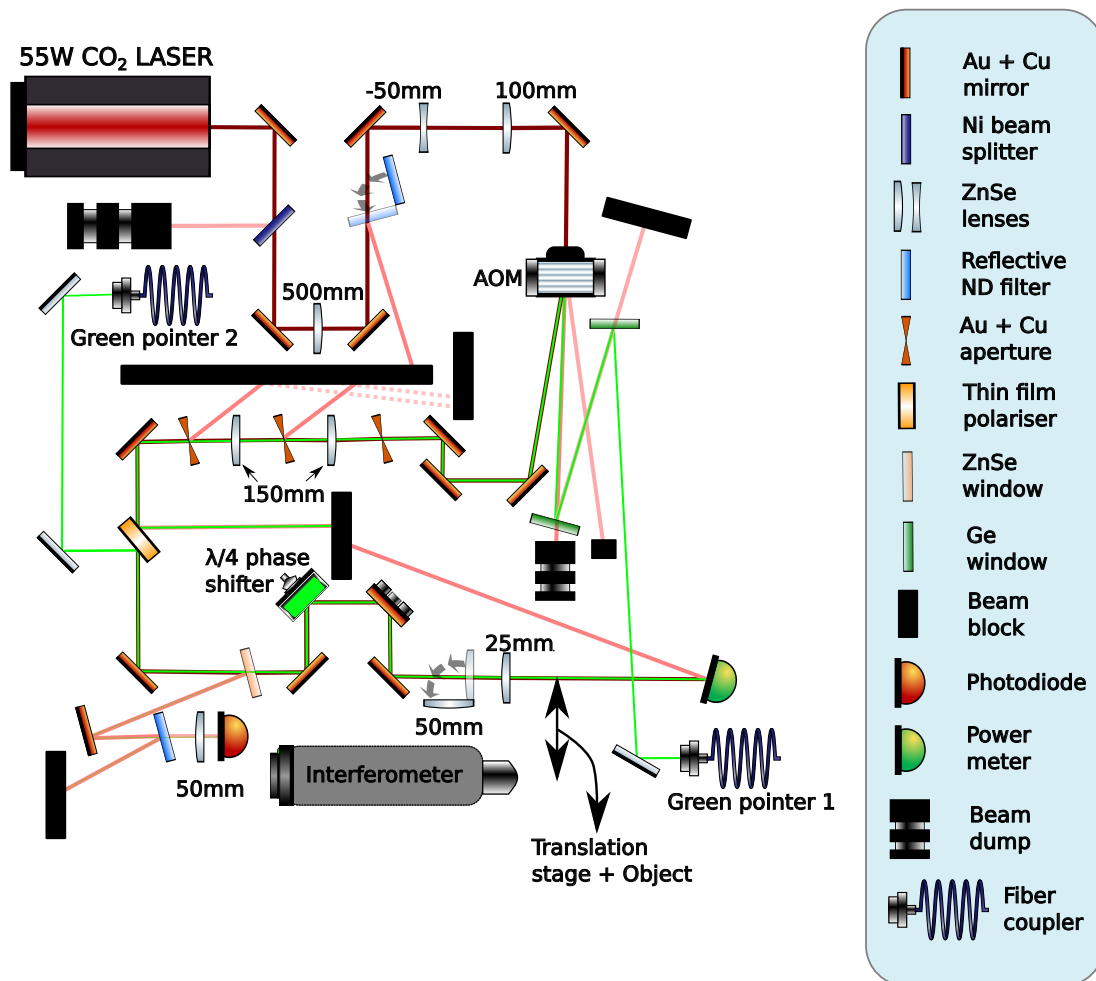


Figure 5.6: The new fibre shooting experiment with green lasers overlay.

The next step is to image the two green beams and the IR beam simultaneously to detect any correlations in their drifts. If such a correlation is detected, we can accordingly use the visible beams to stabilise the IR one. We however could not take this measurement as the experiment

had to be moved to a different building. Once this process is done, we plan to measure the correlation in beam drifts in the new ambience.

### 5.3.2 New python experimental control

The previous experimental control application was written using MATLAB [42]. It was programmed as a single modular application when the experiment was conceived. One could perform very basic operations with this such as object alignment, setting pulse characteristics, and reconstruction of surface profile using the white light interferometer. Owing to its single threaded nature, if any of the devices crashed during the experiment, entire program would crash. Furthermore, it was quite difficult to implement new and complex features into it without having to make major changes. Thus, we decided to build a new experimental control application that is robust and powerful. For this purpose, we choose Python programming language as it is powerful, free, open source, and has a large community.

The new python application has the following features:

- **Modular:** Each device in the experiment is considered as an independent module. If any device is removed, added, or modified, only its specific module must be changed. Thus, complex features can be added easily.
- **Multi threaded:** Each module is run on a separate thread. Thus, if any device crashes, its respective thread is killed, and not the entire program.
- **Independent GUI:** The graphical user interface is designed using QT5 <sup>2</sup>, and is independent of the back-end. Thus, any glitch in GUI has no affect on the experiment. Furthermore, experiment can be automated using custom programmes and “shot sequences” via the back-end.
- **Auto calibration:** Important parameters such as AOM diffraction efficiency, interferometer background, stage calibration, etc. are automated.
- **Master configuration:** All important parameters are stored in a separate config file. Major changes can be applied with minimal effort.

With these features, one can implement complex algorithms for solving various problems. Some ideas, and plans are discussed in chapter 6.

---

<sup>2</sup><https://www.qt.io/qt-for-python>

# Chapter 6

## Conclusion and outlook

Summarising the work done in this thesis, monolayers of MoSe<sub>2</sub> were successfully transferred onto the end facet of a single mode optical fibre. An experiment was designed and implemented to perform laser spectroscopy on the fibre-monolayer assembly at liquid nitrogen temperature. Exciton resonance properties were obtained for our specific flake from 80 K to 135 K. In order to satisfy the general research interest of fabricating micro mirrors on optical fibres and glass substrates, a new spatial mode filter was designed and implemented in the CO<sub>2</sub> laser shooting experiment. The experiment was thoroughly characterised using a physical model of laser ablation. Various applications of laser-dot milling using multiple shots were described. The observed challenges regarding the multi-shot technique were presented. To expand the capabilities of our setup, a new experimental control application was written and implemented using Python programming language.

For our monolayer TMDC, at 80 K, the non-radiative broadening was found to be about 4 times greater than the radiative one. Thus, to reach the condition 2.5, we must cool down the sample further using liquid helium, and perform spectroscopy. We predict this will suppress decay channels through phonons, leading to better excitonic response. Since the resonance can shift further towards the blue side of spectrum, we must use a different laser that can be scanned further towards the lower wavelength region. A new spectroscopy setup must be built for this purpose. To further enhance the optical response, one can also use a stack of monolayers: hBN – TMDC – hBN as shown in [54].

The new python experimental control allows new devices to be added with minimal effort. One such upgrade that must be implemented is to motorise the goniometer stages. In combination with an efficient algorithm for detecting the fibre edges, one can automate the shooting procedure to obtain large amounts of data with minimal human intervention. With the new switchable interferometer, one can use the broadband light source for fine alignment and the narrowband LED for fast reconstruction. With this capability to obtaining large amount of data, we can implement complex algorithms to solve various problems.

A neural network must be designed to generate a basis set for laser dot-milling. This must include all parameters such as depth, width, ellipticity, substrate material, etc. With a universal basis set of shots, and the fast surface reconstruction, a feedback mechanism can be implemented for local correction of surface profile. Thus, we can fabricate custom profiles of very high quality in a short period of time. With each component in the setup computerised, cutting edge techniques such as reinforcement learning can be implemented to make the computer learn non-linearities present in our experiment.

With TMDC monolayers on optical fibres, and our capability to fabricate microstructures, the next, and the final step in our experiment is to put the two together as mentioned in section 2.3 to generate a single photon source.



# Appendix A

## Fibre shooting process

### A.1 New python application

Figure A.1 shows the new graphical user interface of experimental control. From the top left of the main window, going down, one first finds the stage control. Here one can move the motorised translational stages. Below is the interferometer difference values, which are the incremental values for the stage to move the object from the centre of interferometer to the laser beam. Below that, one finds various shooting settings.

On second column in the application, an autofocus algorithm is implemented to bring the object into focus. Below, one finds various settings to control the camera, and the interferometer piezo focussing stage for surface reconstruction. Next to the main application is a live preview of a successfully shot SM fibre, illuminated with a halogen lamp.

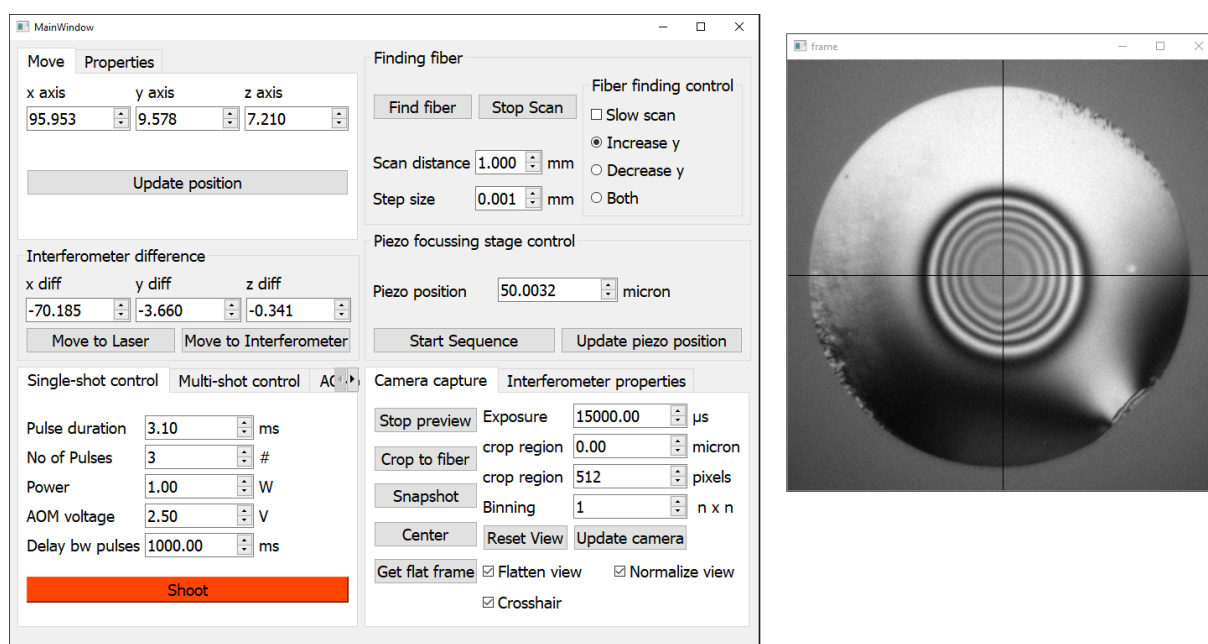


Figure A.1: The new python experimental control application. On the right, one can also see a live preview of a shot single mode fibre.

## A.2 Procedure

### Mounting

In the laboratory, a 3-axis motorised translation stage<sup>1</sup> is used to position the object of interest (fibre or substrate) precisely. Fibres are mounted using specially designed holders onto manual goniometer stages. These allow precise angular alignment of the fibres. The design of mounting structure can be found in [43]. A typical setup is shown in Figure A.2.

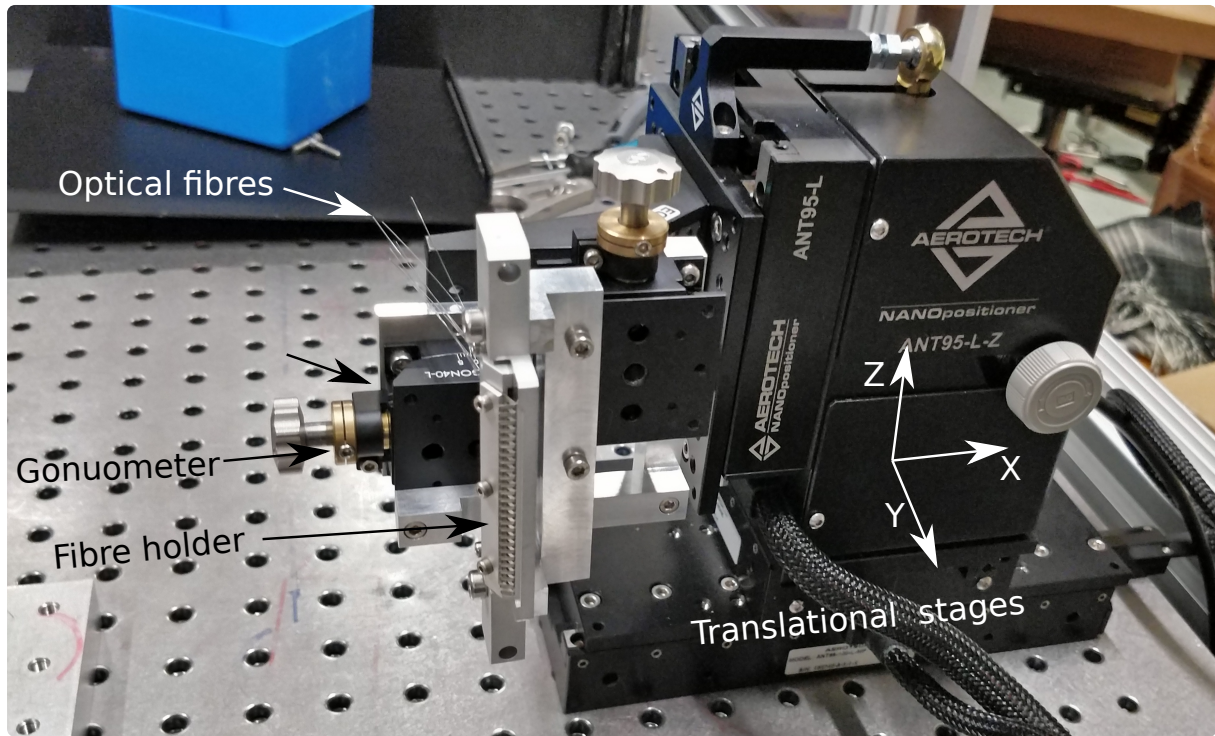


Figure A.2: Mounting of the object in CO<sub>2</sub> fibre shooting experiment. Fibres are held by a fibre holder, which is mounted onto a pair of goniometers. 3 axis motorised translation stages are used for positioning of the fibres.

### Single shot fabrication procedure

Following is step-by-step description of single shot fabrication process:

1. Mount the object of interest (fibre or substrate) onto the goniometers.
2. Start camera preview using the application.
3. Approximately place the object in camera field of view.
4. Use the “**Find fibre**” button in the app to bring the object into focus.
5. Align the object with cross hair using the centre button.
6. Tweak the goniometers to remove any interference fringes on the object. This aligns the surface with the interferometer axis.
7. Set the required shooting parameters – power, pulse duration, etc.
8. Use “**move to laser**” button to move the object into shooting position.

---

<sup>1</sup>Aerotech ANT series

9. **Shoot!**

10. Bring the object back to interferometer.
11. Check if the shot is centred with cross hair. If not, tweak the difference values appropriately for subsequent shots.
12. Reduce the y-position of the stage by about 3 micron, and start the reconstruction sequence.
13. Use appropriate surface reconstruction algorithm from the computer to obtain the profile.



## Appendix B

# Displaced shots illustrations

This appendix shows some shoot patterns and their respective results. Here, I only show the data obtained from SM fibres of  $125\ \mu\text{m}$  diameter. The behaviour was very similar with a substrate. I shot a ring of radius  $20\ \mu\text{m}$  with 16 shots, equally spaced from each other. The first pattern is illustrated in Figure B.1 with the fibre as reference.

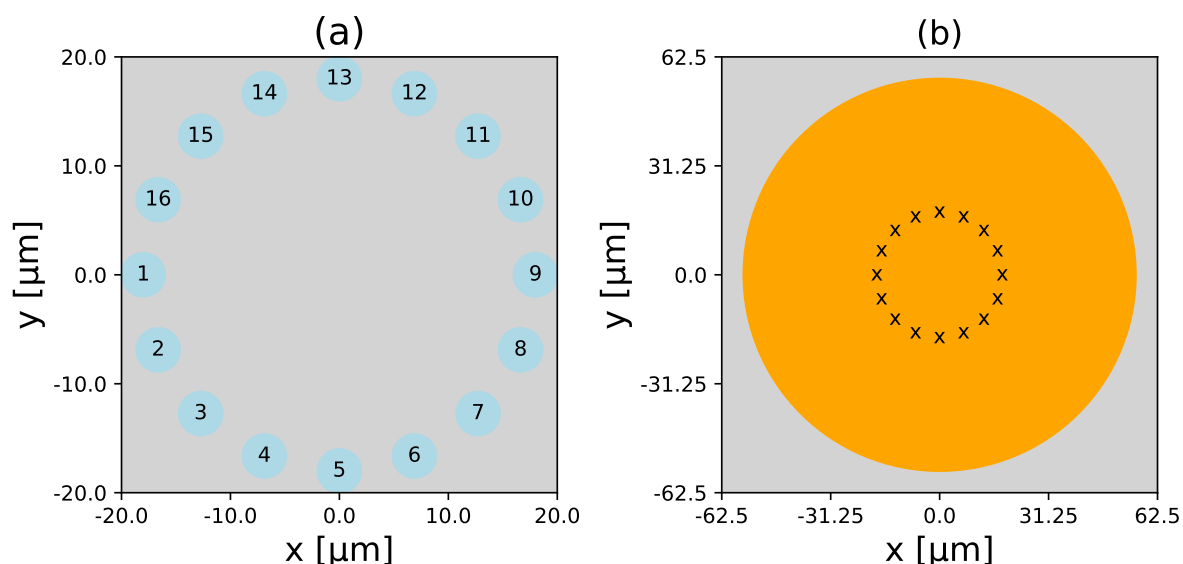


Figure B.1: (a) Ring of shots with diameter of  $40\ \mu\text{m}$ . Numbers represent the shot order. Blue disks are only there for aesthetic purpose, and do not represent any physical quantity. (b) SM fibre of  $125\ \mu\text{m}$  diameter cladding as reference.

For an ideal system, the resulting profile had to be same for all six patterns shown in Figure B.3. But, we observed some differences. An empirical model 5.3 from subsection 5.2.3 is also illustrated that qualitatively resembles the observation, but not quantitatively. I have plotted the relation Equation B.1 instead of the raw profile for better visualisation:

$$f(x, y) = \cos(2\pi/0.2 \cdot S(x, y)) \quad (\text{B.1})$$

where  $S(x, y)$  is the surface profile reconstructed from the interferometer. This is done to reproduce the live view from the interferometer. Horizontal and vertical slices of the actual

profile is illustrated for the first pattern in Figure B.2. The slices are not illustrated for all patterns in thesis as they do not offer any more insight on paper.

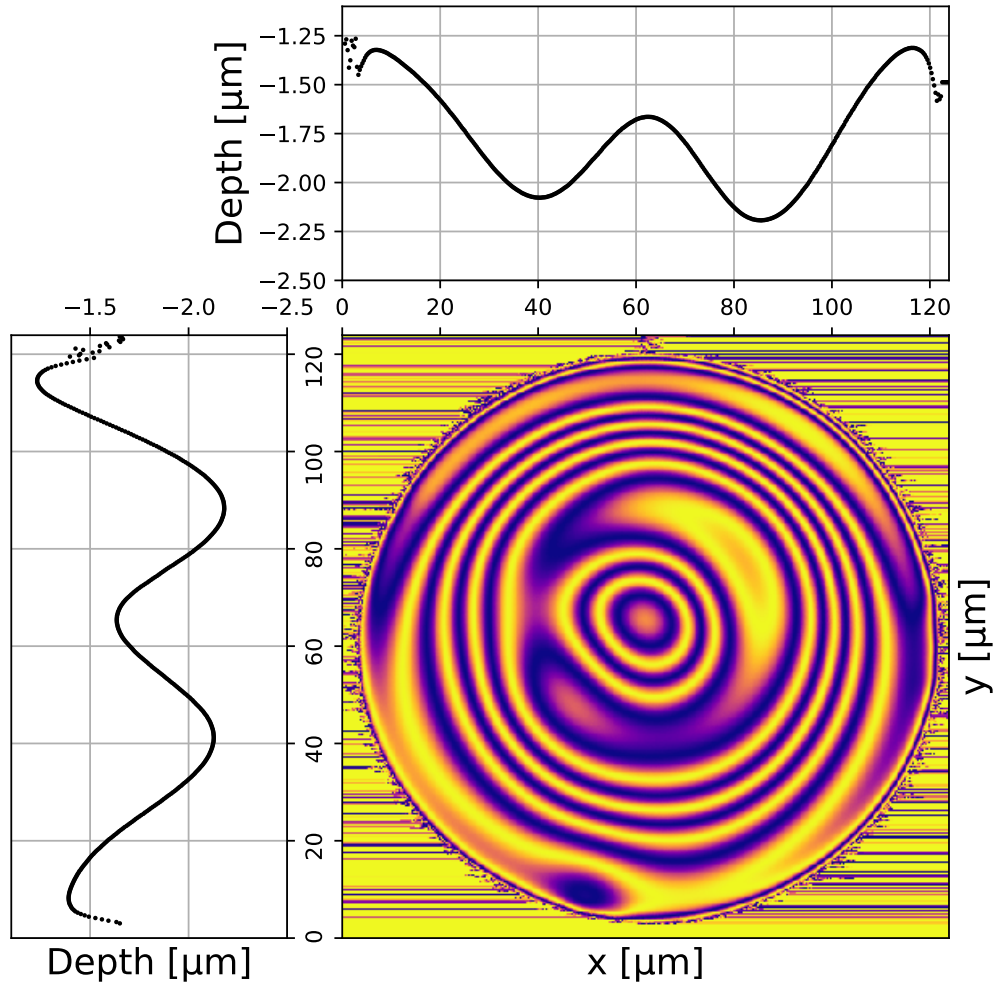


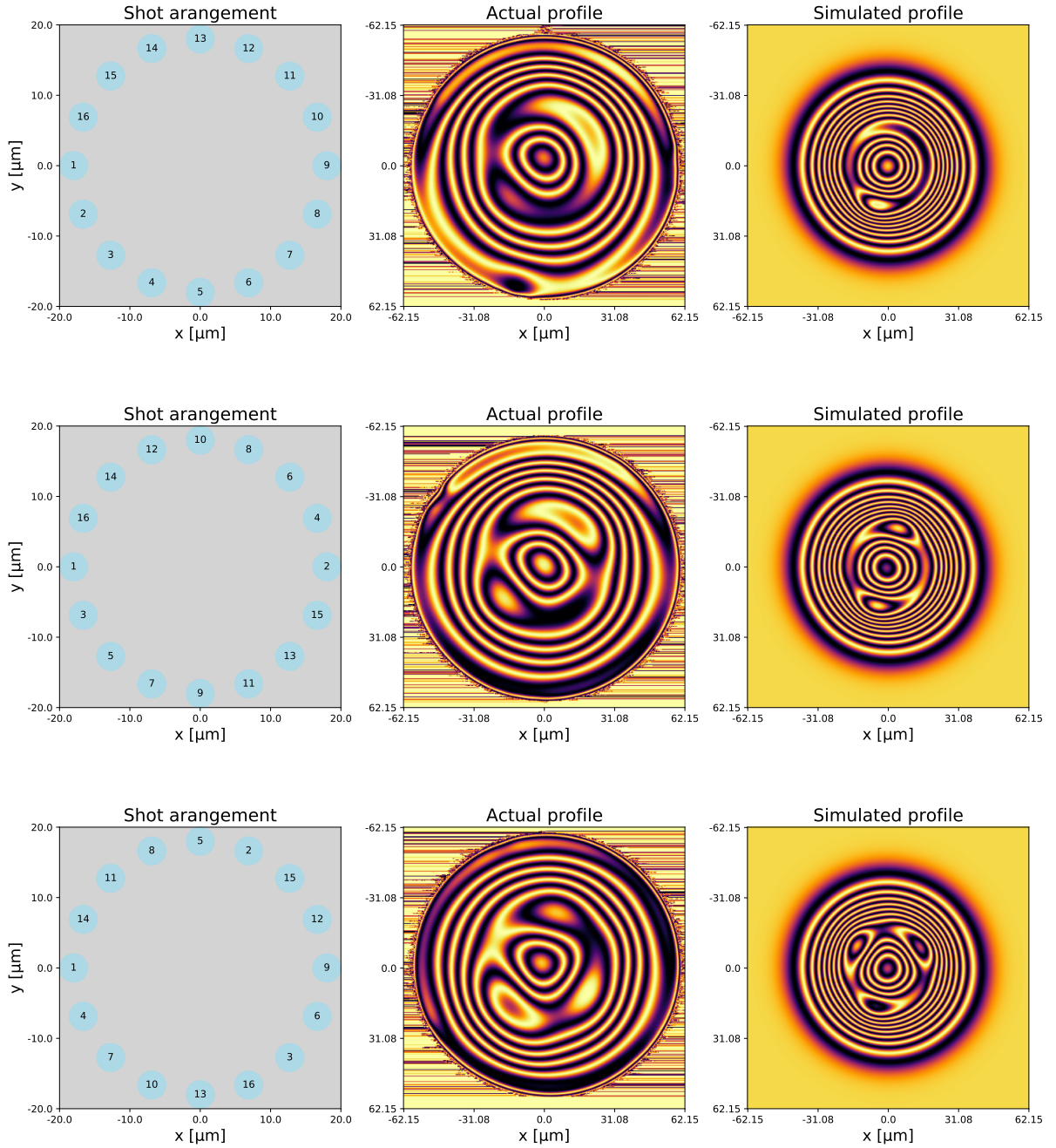
Figure B.2: This figure illustrates the shot profile based on Equation B.1. Central row and column are plotted with real scale on top, and to the left respectively.

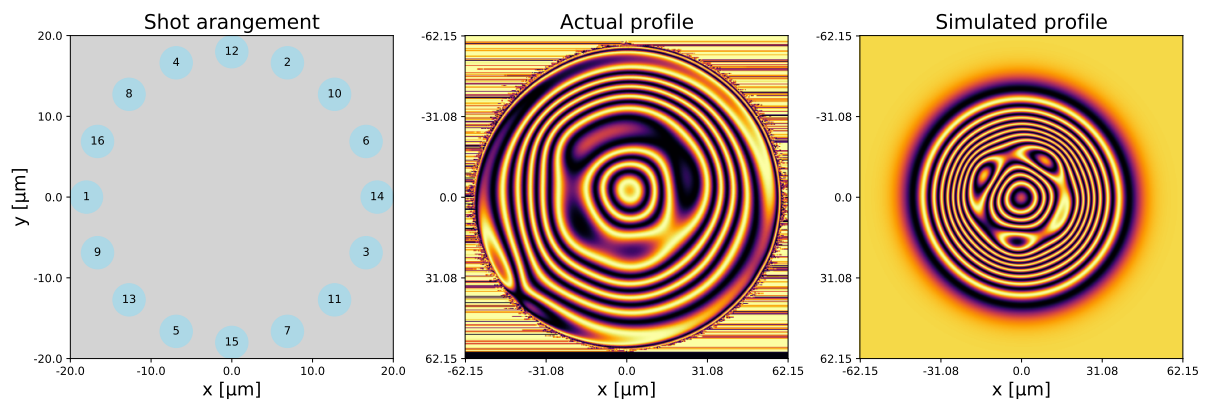
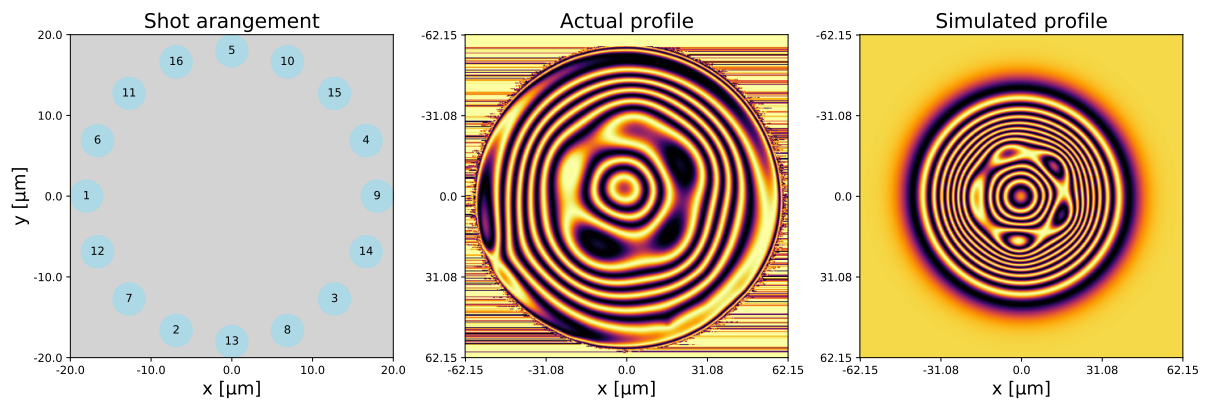
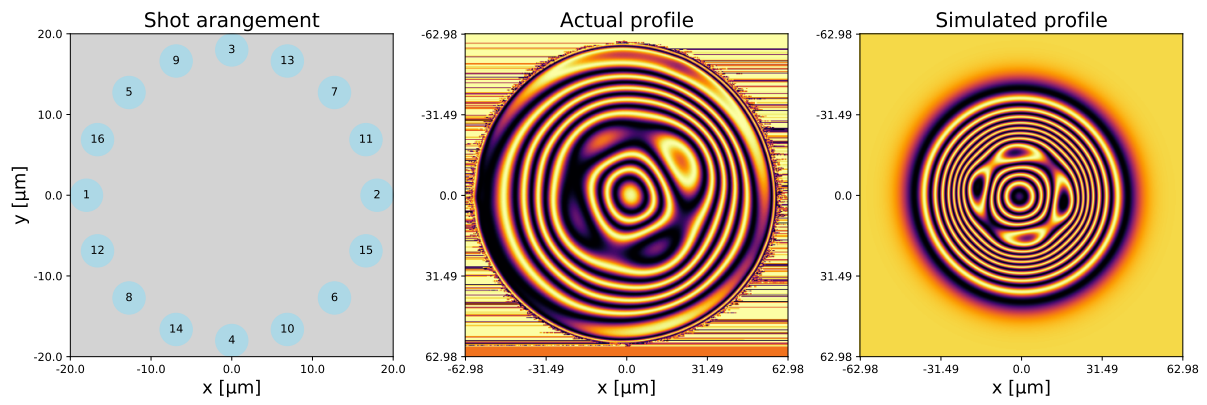
We tried a lot of patterns over the course of my masters, and here I illustrate six of them. Each pattern consists of 16 identical shots placed on a circle of radius  $20\ \mu\text{m}$ . The shot parameters are shown in table Table B.1. Figure B.3 illustrates the six patterns of displaced shots on a SM fibre. Similar results were observed on a substrate as well.

Parameter	Range
Power (P)	1 W
Pulse Duration ( $\tau_{ON}$ )	4.5 ms
Beam waist (a)	70 $\mu\text{m}$
No. of pulses	1
Delay bw. pulses ( $\tau_{OFF}$ )	3 s
Dist. from centre ( $d_0$ )	20 $\mu\text{m}$

Table B.1: Parameters used for all trials in Figure B.3.

Figure B.3: The series of figures below illustrates various shot orders, and their results. The left most column shows the arrangement of shots, and their order. Central column illustrates the shot profile based on Equation B.1. The last column shows a simulation from Equation 5.3 with Equation B.1.





# References

- [1] Max Planck. “Ueber das Gesetz der Energieverteilung im Normalspectrum”. In: *Annalen der Physik* 309.3 (1901), pp. 553–563. DOI: <https://doi.org/10.1002/andp.19013090310>.
- [2] A. Einstein. “Über einen die Erzeugung und Verwandlung des Lichtes betreffenden heuristischen Gesichtspunkt”. In: *Annalen der Physik* 322.6 (1905), pp. 132–148. DOI: <https://doi.org/10.1002/andp.19053220607>.
- [3] GILBERT N. LEWIS. “The Conservation of Photons”. In: *Nature* 118.2981 (1926), pp. 874–875. ISSN: 1476-4687. URL: <https://doi.org/10.1038/118874a0>.
- [4] C. K. Hong, Z. Y. Ou, and L. Mandel. “Measurement of subpicosecond time intervals between two photons by interference”. In: *Phys. Rev. Lett.* 59 (18 1987), pp. 2044–2046. DOI: 10.1103/PhysRevLett.59.2044.
- [5] Fabian Ripka et al. “A room-temperature single-photon source based on strongly interacting Rydberg atoms”. In: *Science* 362.6413 (2018), pp. 446–449. ISSN: 0036-8075. DOI: 10.1126/science.aau1949. eprint: <https://science.sciencemag.org/content/362/6413/446.full.pdf>. URL: <https://science.sciencemag.org/content/362/6413/446>.
- [6] D B Higginbottom et al. “Pure single photons from a trapped atom source”. In: *New Journal of Physics* 18.9 (2016), p. 093038. DOI: 10.1088/1367-2630/18/9/093038. URL: <https://doi.org/10.1088/1367-2630/18/9/093038>.
- [7] Juliane Bahe et al. “A single photon source based on NV centers in diamond nanocrystals”. In: *CLEO/Europe and EQEC 2009 Conference Digest*. Optical Society of America, 2009, EB<sub>P</sub>2. URL: [http://www.osapublishing.org/abstract.cfm?URI=EQEC-2009-EB\\_P2](http://www.osapublishing.org/abstract.cfm?URI=EQEC-2009-EB_P2).
- [8] Pascale Senellart, Glenn Solomon, and Andrew White. “High-performance semiconductor quantum-dot single-photon sources”. In: *Nature Nanotechnology* 12.11 (2017), pp. 1026–1039. ISSN: 1748-3395. DOI: 10.1038/nnano.2017.218. URL: <https://doi.org/10.1038/nnano.2017.218>.
- [9] K. S. Novoselov et al. “Electric Field Effect in Atomically Thin Carbon Films”. In: *Science* 306.5696 (2004), pp. 666–669. ISSN: 0036-8075. DOI: 10.1126/science.1102896. eprint: <https://science.sciencemag.org/content/306/5696/666.full.pdf>. URL: <https://science.sciencemag.org/content/306/5696/666>.
- [10] J. Frenkel. “On the Transformation of light into Heat in Solids. I”. In: *Phys. Rev.* 37 (1 1931), pp. 17–44. DOI: 10.1103/PhysRev.37.17. URL: <https://link.aps.org/doi/10.1103/PhysRev.37.17>.
- [11] Dominik S. Wild et al. “Quantum Nonlinear Optics in Atomically Thin Materials”. In: *Phys. Rev. Lett.* 121 (12 2018), p. 123606. DOI: 10.1103/PhysRevLett.121.123606. URL: <https://link.aps.org/doi/10.1103/PhysRevLett.121.123606>.
- [12] Fabian Mayer. “Spektroskopie einer Monolage MoSe<sub>2</sub> bei kryostatistischen Temperaturen”. BA Thesis. 53113, Bonn, Germany: Rheinischen Friedrich-Wilhelms-Universität Bonn, 2020.
- [13] Anica Hamer. “Spectroscopy of MoSe<sub>2</sub> Monolayers at Cryogenic Temperatures”. BA Thesis. 53113, Bonn, Germany: Rheinischen Friedrich-Wilhelms-Universität Bonn, 2019.

- [14] Pascal Kobel, Moritz Breyer, and Michael Köhl. “Deterministic spin-photon entanglement from a trapped ion in a fiber Fabry–Perot cavity”. In: *npj Quantum Information* 7.1 (2021), p. 6. ISSN: 2056-6387. DOI: 10.1038/s41534-020-00338-2. URL: <https://doi.org/10.1038/s41534-020-00338-2>.
- [15] Felix Rönchen, Thorsten F Langerfeld, and Michael Köhl. “Correlated photon-pair generation in a liquid-filled microcavity”. In: *New Journal of Physics* 21.12 (2019), p. 123037. DOI: 10.1088/1367-2630/ab5daa. URL: <https://doi.org/10.1088/1367-2630/ab5daa>.
- [16] Thorsten F. Langerfeld, Hendrik M. Meyer, and Michael Köhl. “Correlated-photon-pair emission from a cw-pumped Fabry-Perot microcavity”. In: *Phys. Rev. A* 97 (2 2018), p. 023822. DOI: 10.1103/PhysRevA.97.023822. URL: <https://link.aps.org/doi/10.1103/PhysRevA.97.023822>.
- [17] D Hunger et al. “A fiber Fabry–Perot cavity with high finesse”. In: *New Journal of Physics* 12.6 (2010), p. 065038. DOI: 10.1088/1367-2630/12/6/065038. URL: <https://doi.org/10.1088/1367-2630/12/6/065038>.
- [18] A. Nagashima et al. “Electronic Structure of Monolayer Hexagonal Boron Nitride Physisorbed on Metal Surfaces”. In: *Phys. Rev. Lett.* 75 (21 1995), pp. 3918–3921. DOI: 10.1103/PhysRevLett.75.3918. URL: <https://link.aps.org/doi/10.1103/PhysRevLett.75.3918>.
- [19] Andrea Splendiani et al. “Emerging Photoluminescence in Monolayer MoS<sub>2</sub>”. In: *Nano Letters* 10.4 (2010). PMID: 20229981, pp. 1271–1275. DOI: 10.1021/nl903868w. eprint: <https://doi.org/10.1021/nl903868w>. URL: <https://doi.org/10.1021/nl903868w>.
- [20] Weitao Tang, Sushant S Rassay, and Nuggehalli M Ravindra. “Electronic & Optical properties of Transition-Metal Dichalcogenides”. In: *Madridge Journal of Nanotechnology & Nanoscience* 2.1 (July 2017), pp. 58–64. DOI: 10.18689/mjnn-1000111. URL: <https://doi.org/10.18689/mjnn-1000111>.
- [21] Ben Mills. *MoSe<sub>2</sub> structure*. 2007. URL: [https://en.wikipedia.org/wiki/Molybdenum\\_diselenide#/media/File:Molybdenite-3D-balls.png](https://en.wikipedia.org/wiki/Molybdenum_diselenide#/media/File:Molybdenite-3D-balls.png).
- [22] Jose Ángel Silva-Guillén, Pablo San-Jose, and Rafael Roldán. “Electronic Band Structure of Transition Metal Dichalcogenides from Ab Initio and Slater–Koster Tight-Binding Model”. In: *Applied Sciences* 6.10 (2016). ISSN: 2076-3417. DOI: 10.3390/app6100284. URL: <https://www.mdpi.com/2076-3417/6/10/284>.
- [23] Gui-Bin Liu et al. “Three-band tight-binding model for monolayers of group-VIB transition metal dichalcogenides”. In: *Phys. Rev. B* 88 (8 2013), p. 085433. DOI: 10.1103/PhysRevB.88.085433. URL: <https://link.aps.org/doi/10.1103/PhysRevB.88.085433>.
- [24] Philipp Tonndorf et al. “Photoluminescence emission and Raman response of monolayer MoS<sub>2</sub>, MoSe<sub>2</sub>, and WSe<sub>2</sub>”. In: *Opt. Express* 21.4 (2013), pp. 4908–4916. DOI: 10.1364/OE.21.004908. URL: <http://www.opticsexpress.org/abstract.cfm?URI=oe-21-4-4908>.
- [25] Di Xiao, Wang Yao, and Qian Niu. “Valley-Contrasting Physics in Graphene: Magnetic Moment and Topological Transport”. In: *Phys. Rev. Lett.* 99 (23 2007), p. 236809. DOI: 10.1103/PhysRevLett.99.236809. URL: <https://link.aps.org/doi/10.1103/PhysRevLett.99.236809>.
- [26] Di Xiao et al. “Coupled Spin and Valley Physics in Monolayers of MoS<sub>2</sub> and Other Group-VI Dichalcogenides”. In: *Phys. Rev. Lett.* 108 (19 2012), p. 196802. DOI: 10.1103/PhysRevLett.108.196802. URL: <https://link.aps.org/doi/10.1103/PhysRevLett.108.196802>.
- [27] O. D. D. Couto et al. “Charge control in InP/(Ga,In)P single quantum dots embedded in Schottky diodes”. In: *Phys. Rev. B* 84 (12 2011), p. 125301. DOI: 10.1103/PhysRevB.84.125301. URL: <https://link.aps.org/doi/10.1103/PhysRevB.84.125301>.

- [28] Yue Niu et al. “Thickness-Dependent Differential Reflectance Spectra of Monolayer and Few-Layer MoS<sub>2</sub>, MoSe<sub>2</sub>, WS<sub>2</sub> and WSe<sub>2</sub>”. In: *Nanomaterials* 8.9 (2018). ISSN: 2079-4991. URL: <https://www.mdpi.com/2079-4991/8/9/725>.
- [29] Riccardo Frisenda et al. “Micro-reflectance and transmittance spectroscopy: a versatile and powerful tool to characterize 2D materials”. In: *Journal of Physics D: Applied Physics* 50.7 (2017), p. 074002. DOI: 10.1088/1361-6463/aa5256. URL: <https://doi.org/10.1088/1361-6463/aa5256>.
- [30] Han Gyeol Park et al. “Temperature Dependence of the Dielectric Function of Monolayer MoSe<sub>2</sub>”. In: *Scientific Reports* 8.1 (2018), p. 3173. ISSN: 2045-2322. DOI: 10.1038/s41598-018-21508-5. URL: <https://doi.org/10.1038/s41598-018-21508-5>.
- [31] A.M. Fox and D.P.A.M. Fox. *Optical Properties of Solids*. Oxford master series in condensed matter physics. Oxford University Press, 2001. ISBN: 9780198506126.
- [32] Sebastian Huber Sina Zeytinoglu Charlaïne Roth and Atac Imamoglu. “Atomically thin semiconductors as nonlinear mirrors”. In: *Phys. Rev. A* 96 (3 2017), p. 031801. DOI: 10.1103/PhysRevA.96.031801. URL: <https://link.aps.org/doi/10.1103/PhysRevA.96.031801>.
- [33] Malte Selig et al. “Excitonic linewidth and coherence lifetime in monolayer transition metal dichalcogenides”. In: *Ultrafast Phenomena and Nanophotonics XXI*. Ed. by Markus Betz and Abdulhakem Y. Elezzabi. Vol. 10102. International Society for Optics and Photonics. SPIE, 2017, pp. 160–168. DOI: 10.1117/12.2252486. URL: <https://doi.org/10.1117/12.2252486>.
- [34] Ashish Arora et al. “Exciton band structure in layered MoSe<sub>2</sub>: from a monolayer to the bulk limit”. In: *Nanoscale* 7 (48 2015), pp. 20769–20775. DOI: 10.1039/C5NR06782K. URL: <http://dx.doi.org/10.1039/C5NR06782K>.
- [35] Bahaa E. A. Saleh and Malvin Carl Teich. *Fundamentals of Photonics*. John Wiley and Sons, Ltd, 1991. ISBN: 9780471213741.
- [36] E. M. Purcell, H. C. Torrey, and R. V. Pound. “Resonance Absorption by Nuclear Magnetic Moments in a Solid”. In: *Phys. Rev.* 69 (1-2 1946), pp. 37–38. DOI: 10.1103/PhysRev.69.37. URL: <https://link.aps.org/doi/10.1103/PhysRev.69.37>.
- [37] S.I. Pekar. “Theory of electromagnetic waves in a crystal with excitons”. In: *Journal of Physics and Chemistry of Solids* 5.1 (1958), pp. 11–22. ISSN: 0022-3697. DOI: [https://doi.org/10.1016/0022-3697\(58\)90127-6](https://doi.org/10.1016/0022-3697(58)90127-6). URL: <https://www.sciencedirect.com/science/article/pii/0022369758901276>.
- [38] Andres Castellanos-Gomez et al. “Deterministic transfer of two-dimensional materials by all-dry viscoelastic stamping”. In: *2D Materials* 1.1 (2014), p. 011002. DOI: 10.1088/2053-1583/1/1/011002. URL: <https://doi.org/10.1088/2053-1583/1/1/011002>.
- [39] Riccardo Frisenda et al. “Recent progress in the assembly of nanodevices and van der Waals heterostructures by deterministic placement of 2D materials”. In: *Chem. Soc. Rev.* 47 (1 2018), pp. 53–68. DOI: 10.1039/C7CS00556C. URL: <http://dx.doi.org/10.1039/C7CS00556C>.
- [40] Patrick Back et al. “Realization of an Electrically Tunable Narrow-Bandwidth Atomically Thin Mirror Using Monolayer MoSe<sub>2</sub>”. In: *Phys. Rev. Lett.* 120 (3 2018), p. 037401. DOI: 10.1103/PhysRevLett.120.037401. URL: <https://link.aps.org/doi/10.1103/PhysRevLett.120.037401>.
- [41] Madhavakannan Saravanan. “Mode-matched fiber fabry perot cavities for quantum technologies”. MA thesis. 53113, Bonn, Germany: Rheinischen Friedrich-Wilhelms-Universität Bonn, 2020.
- [42] Michael Kubista. “A New Fiber Mirror Production Setup”. MA thesis. 53113, Bonn, Germany: Rheinischen Friedrich-Wilhelms-Universität Bonn, 2017.

- [43] Leon Reiffert. “High finesse fiber cavities for quantum computing”. MA thesis. 53113, Bonn, Germany: Rheinischen Friedrich-Wilhelms-Universität Bonn, 2020.
- [44] Ricky K. Nubling and James A. Harrington. “Hollow-waveguide delivery systems for high-power, industrial CO<sub>2</sub> lasers”. In: *Appl. Opt.* 35.3 (1996), pp. 372–380. DOI: 10.1364/AO.35.000372. URL: <http://ao.osa.org/abstract.cfm?URI=ao-35-3-372>.
- [45] Pia Johanna Fürtjes. “Integrated Fibre Cavity for Quantum Networks”. MA thesis. 53113, Bonn, Germany: Rheinischen Friedrich-Wilhelms-Universität Bonn, 2018.
- [46] Michael D. Feit and Alexander M. Rubenchik. “Mechanisms of CO<sub>2</sub> laser mitigation of laser damage growth in fused silica”. In: *Laser-Induced Damage in Optical Materials: 2002 and 7th International Workshop on Laser Beam and Optics Characterization*. Ed. by Gregory J. Exarhos et al. Vol. 4932. International Society for Optics and Photonics. SPIE, 2003, pp. 91–102. DOI: 10.1117/12.472049. URL: <https://doi.org/10.1117/12.472049>.
- [47] Patrik Holmberg. “Laser processing of Silica based glass”. PhD thesis. 106 91 Stockholm, Sweden: Department of Applied Physics, KTH – Royal Institute of Technology, 2015.
- [48] Rei Kitamura, Laurent Pilon, and Mirosław Jonasz. “Optical constants of silica glass from extreme ultraviolet to far infrared at near room temperature”. In: *Appl. Opt.* 46.33 (2007), pp. 8118–8133. DOI: 10.1364/AO.46.008118. URL: <http://ao.osa.org/abstract.cfm?URI=ao-46-33-8118>.
- [49] S. I. Anisimov, N. M. Bityurin, and B. S. Luk’yanchuk. “Models for Laser Ablation”. In: *Photo-Excited Processes, Diagnostics and Applications: Fundamentals and Advanced Topics*. Ed. by A. Peled. Boston, MA: Springer US, 2003, pp. 121–159.
- [50] Manuel Uphoff et al. “Frequency splitting of polarization eigenmodes in microscopic Fabry–Perot cavities”. In: *New Journal of Physics* 17.1 (2015), p. 013053. DOI: 10.1088/1367-2630/17/1/013053. URL: <https://doi.org/10.1088/1367-2630/17/1/013053>.
- [51] Anthony E. Siegman. “Lasers”. In: University Science Books, 1990. ISBN: 0935702113.
- [52] F. Laguarda, N. Lupon, and J. Armengol. “Optical glass polishing by controlled laser surface-heat treatment”. In: *Appl. Opt.* 33.27 (1994), pp. 6508–6513. DOI: 10.1364/AO.33.006508. URL: <http://ao.osa.org/abstract.cfm?URI=ao-33-27-6508>.
- [53] J. Schwider et al. “Digital wave-front measuring interferometry: some systematic error sources”. In: *Appl. Opt.* 22.21 (1983), pp. 3421–3432. DOI: 10.1364/AO.22.003421. URL: <http://ao.osa.org/abstract.cfm?URI=ao-22-21-3421>.
- [54] Giovanni Scuri et al. “Large Excitonic Reflectivity of Monolayer MoSe<sub>2</sub> Encapsulated in Hexagonal Boron Nitride”. In: *Phys. Rev. Lett.* 120 (3 2018), p. 037402. DOI: 10.1103/PhysRevLett.120.037402. URL: <https://link.aps.org/doi/10.1103/PhysRevLett.120.037402>.

# Acknowledgements

First of all, I want to thank Prof. Dr. Michael Köhl for providing me these wonderful projects. Thank you for supervising me through both “perfect” and “crisis” modes, entrusting me with all the freedom in the experiments, and of course for being a source of inspiration throughout my masters. I want to also thank you for getting me a scholarship, which let me to concentrate completely on the experiments, having not to worry about my finances.

Furthermore, I want to thank Prof. Dr. Stefan Linden, whose expertise on TMDC allowed me to take up this wonderful project. I want to thank Yuhao Zhang for teaching me the process of monolayer fabrication and transfer, and Alexander Faßbender for getting the high power apertures gold coated.

Special gratitudes to Dr. Frank Vewinger for being Frank!!!

A very special thanks goes to Thorsten Langerfeld who supervised me with the TMDC part of my thesis. Academically, you were always available for discussions related to my projects, greatly shaping my work. Also, thank you for proofreading this thesis, and supporting me in the lab with any problems. Finally, of course, as a friend who was always available during the late nights in pubs, and the desperate times of a pandemic.

I would also like to thank Leon Reiffert, who introduced me to the fibre shooting experiment, and was always there when troubleshooting was required. Gratitudes to Dr. Akos Hoffmann for helping me with all electronics challenges. I want to also thank the members of fibre lab: Wolfgang Alt, Hannes Pfeifer, Deepak Pandey, Carlos Saavedra Salazar, Lukas Tenbrake, and others for all the discussions we had that helped me during the experiments.

Special thanks goes to the members of “prep lab” and “meme lab”: Jonas Schmitz, Felix Rönchen, Steffen Gohlke (+ proofreading), Tobias Kree, Andreas von Haaren, Valentin Jonas, Martin Link, and Moritz Scharfstädt for all the stimulating discussions that greatly helped this work, and the “socially distant social gatherings”<sup>1</sup> that made the pandemic a bit more bearable. Also, thanks for proofreading this thesis! As a whole, I would like to thank my entire group, whose friendly atmosphere made working on my thesis not feel as a chore. All the lunch time discussions contributed a lot to my work.

Of course, my gratitude goes to my friends from lectures and my dorm: Kirankumar K. U., Anna Sidorenko, Alejandro Godinez Sandi, Andreea Lefterovici, Pedro Castro Pérez, Madhavakkannan Saravanan, Pooja Malik, Divya Pal, and others who were there with me since the first day of my masters. Without you all, the journey would have been bland.

Finally, gratitudes to Lucky and my parents – who by now thoroughly know what an optical fibre resonator is! Without all your support and sponsoring, this masters would not have been possible!

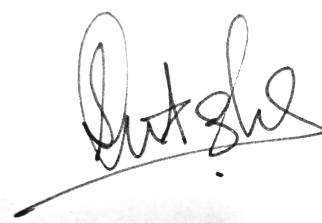
---

<sup>1</sup>I cannot thank coffee and kölsch enough for sustaining me throughout.

I hereby declare that the work presented here was formulated by myself and that no sources or tools other than those cited were used.

Bonn, 14-03-2021

Signature:

A handwritten signature in black ink, appearing to read 'Ditzel', written over a horizontal line.